

Investigation into lossless hyperspectral image compression for satellite remote sensing

NorRizuan Mat Noor and Tanya Vladimirova*

*Department of Engineering, University of Leicester, Leicester, LE1 7RH, UK
(Received 14 December 2011; accepted 11 November 2012)*

Hyperspectral sensors acquire images in many, very narrow, contiguous spectral bands throughout the visible, near-infrared (IR), mid-IR and thermal IR portions of the spectrum, thus requiring large data storage on board the satellite and high bandwidth of the downlink transmission channel to ground stations. Image compression techniques are required to compensate for the limitations in terms of on-board storage and communication link bandwidth. In most remote-sensing applications, preservation of the original information is important and urges studies on lossless compression techniques for on-board implementation. This article first reviews hyperspectral spaceborne missions and compression techniques for hyperspectral images used on board satellites. The rest of the article investigates the suitability of the integer Karhunen–Loève transform (KLT) for lossless inter-band compression in spaceborne hyperspectral imaging payloads. Clustering and tiling strategies are employed to reduce the computational complexity of the algorithm. The integer KLT performance is evaluated through a comprehensive numerical experimentation using four airborne and four spaceborne hyperspectral datasets. In addition, an implementation of the integer KLT algorithm is ported to an embedded platform including a digital signal processor (DSP). The DSP performance results are reported and compared with the desktop implementation. The effects of clustering and tiling techniques on the compression ratio and latency are assessed for both desktop and the DSP implementation.

1. Introduction

In hyperspectral remote sensing, the terms *imaging spectroscopy*, *imaging spectrometry*, and *hyperspectral imaging* are often used interchangeably. The common definition for those terms is ‘the simultaneous acquisition of spatially co-registered images, in many narrow, spectrally contiguous bands, measured in calibrated radiance units, from a remotely operated platform’ (Schaepman et al. 2009). Hyperspectral sensors acquire images throughout the visible, near-infrared (IR), mid-IR, and thermal IR bands of the electromagnetic spectrum (Lillesand et al. 2008). A hyperspectral image is represented by three components, as shown in Figure 1: the width x in pixels; the height y in pixels; and a third component, additional to the *spatial components*, referred to as the *spectral component*, λ . This is given in nanometres (nm). The terms *wavelength* or *band number* are also used in the literature to denote the spectral component.

Hyperspectral images have been used for various applications that require a large number of spectral bands to be taken, such as vegetation analysis (Green et al. 2008), disaster monitoring (Zhang et al. 2011), military purposes (Peter and Gary 2006), etc. As the number of spectra increases, the amount of data to be transmitted back to the Earth increases too—which requires data compression to be incorporated in the imaging payload.

* Corresponding author. Email: tv29@le.ac.uk

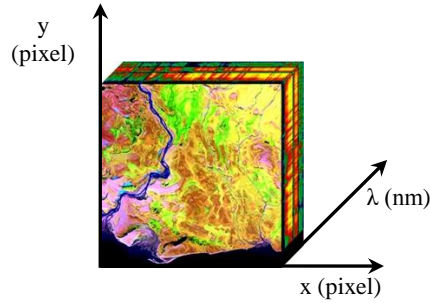


Figure 1. Hyperspectral image representation.

The number of bands that could be captured is used to differentiate between hyperspectral and multispectral imaging. The ‘classical definition’ of hyperspectral imaging is that the number of bands involved is more than 10, and any lower than that is referred to as multispectral imaging (Borengasser et al. 2008a; Schaepman et al. 2009). However, the number of spectral bands is also defined to be in the range of 100 bands in some literature sources (Navulur 2007; Lillesand et al. 2008). In addition to that, the contiguity among bands and its spectral resolution (bandwidth) are also becoming an important feature of hyperspectral imaging that is different from multispectral imaging (Shippert 2003; Schaepman 2007). Hyperspectral images are said to have a very high spectral resolution, providing a better diagnostic capability for object detection, classification, and discrimination than multispectral images (Qian et al. 2008).

With the number of spectral bands growing fast, hyperspectral images result in a very large data volume, requiring increased data storage and a high-bandwidth downlink transmission channel, which increases spacecraft cost. For example, a single image captured by the Airborne Visible/Infrared Imaging Spectrometer (AVIRIS) occupies 134 MB of storage. Image compression has become an effective solution in reducing the image data volume, which is cheaper than using a larger on-board storage and higher speed downlink communication. Other efforts to overcome this problem, such as having multiple ground stations and using a cross-linked distributed satellite system, seem to be practical but also rather costly.

This article first presents an analytical review of hyperspectral spaceborne missions and compression techniques used on board satellites. The remainder of the article investigates the suitability of the integer Karhunen–Loève transform (KLT) (Hao and Shi 2003) for lossless inter-band compression in hyperspectral imaging payloads. The results of a substantial modelling experiment are presented. Design space exploration is carried out to investigate the impact of tiling and clustering techniques on the performance of the integer KLT algorithm. In addition, an implementation of the algorithm is ported to an embedded digital signal processor (DSP) and performance results are reported. Two types of test data are used in the experiments – airborne (AVIRIS) (NASA-JPL 2010b, 2010a) and spaceborne (Hyperion) (USGS 2011) hyperspectral images.

The article is structured as follows: Section 2 gives an introduction to hyperspectral image compression. Section 3 reviews hyperspectral spaceborne missions with a focus on on-board image compression and image processing. Section 4 is an overview of the integer KLT algorithm and the clustering and tiling techniques. Design space exploration of the integer KLT algorithm is discussed in Section 5. Section 6 presents experimental results based on prototyping the algorithm on an embedded DSP platform. Finally, conclusions are given in Section 7.

2. Hyperspectral image compression: an introduction

Compression of hyperspectral imagery adds a third dimension to compressing two-dimensional (2D) digital images (Figure 1). The availability of a large number of spectralbands introduces spectral (inter-band) redundancy in addition to the spatial (intra-band)redundancy present in 2D digital images. Spectral redundancy is due to the correlation (ordependence) present between different spectral bands, whereas spatial redundancy is due tothe correlation between neighbouring pixels in a spectral band (Rabbani and Jones 1991). When compressing hyperspectral images, both types of redundancy need to be removed in order to achieve a good compression performance via a lossless or lossy process.

In most of the cases, spectral decorrelation is performed first, followed by spatialdecorrelation used in 2D image compression as depicted in Figure 2. Spectraldecorrelation aims to reduce the spectral redundancy that exists between bands, whereas spatial decorrelation aims to reduce the spatial redundancy within a band. This schemehas been used widely in remote sensing (Qian and Fowler 2007; Blanes and Serra-Sagristà 2009; Yu et al. 2009; Mat Noor et al. 2010), as well as in medical applications (Yodchanan et al. 2006a; Yodchanan et al. 2006b; Yodchanan 2008)for three-dimensional (3D) medicaldata.

Both spectral and spatial decorrelation can be performed by either a lossless or a lossytransform, as shown in Figure 2. To achieve an overall lossless compression process, both the spectral and the spatial decorrelation stages should utilize lossless transformations. On the other hand, an overall lossy compression process can utilize not only lossy spectral and lossy spatial decorrelation modules (Zhang et al. 2009), but can also have one of the stages executed as lossless, e.g. using a lossless spectral decorrelation module and a lossy spatial decorrelation module (Baizert et al. 2001; Zhou et al. 2006).

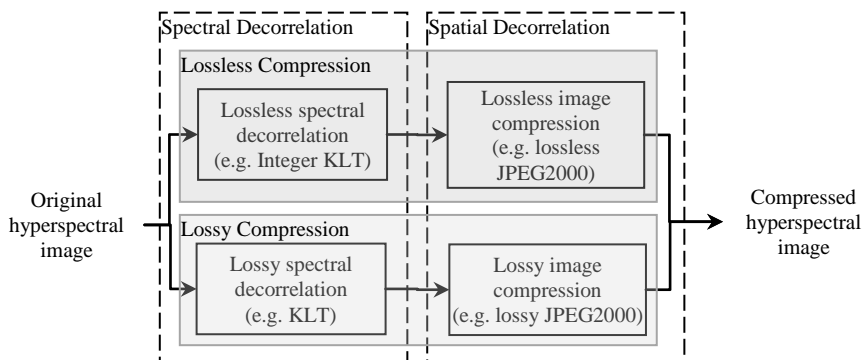


Figure 2. Data flow for hyperspectral image compression.

Different methods have been proposed for hyperspectral data compression (Pickering and Ryan 2006), such as (1) predictive coding, e.g. differential pulse code modulation (DPCM) (Mielikainen and Toivanen 2003), Consultative Committee for Space Data Systems (CCSDS) lossless multispectral and hyperspectral image compression standard (Hopson et al. 2012); (2) vector quantization (VQ) (Ying and Pearlman 2007); and (3) transform coding, e.g. KLT (Penna et al. 2006), discrete cosine transform (DCT) (Khayam 2003), and wavelet transforms (Christophe et al. 2008). VQ methods can be seen as coding of the hyperspectral image in a cube form, where spatial and spectral decorrelations are processed in one single stage. Predictive and transform coding methods have been used to tackle both spectral and spatial decorrelation.

The early hyperspectral image compression studies were based on DPCM (Pickering and Ryan 2006). This predictive coding technique predicts a current pixel value using the

neighbouring pixels and makes use of the difference between the real and predicted values (Roger and Cavenor 1996; Aiazzi et al. 1999). DPCM can be employed for spatial, spectral, and spectral–spatial decorrelation. Spatial predictive methods have been upgraded to perform inter-band compression via increasing the size of the neighbourhood from 2D to 3D. However, according to Wang and Sayood (2006), the direct extension from 2D to 3D may not always provide tangible benefits, and sometimes can prove to be detrimental. Therefore, it is necessary to develop predictors that are specialized for 3D hyperspectral images.

Vector quantization is a form of pattern recognition where an input pattern (i.e. the hyperspectral image) is ‘approximated’ by a predetermined set of standard patterns (Gersho and Gray 1992). The set of standard patterns is also known as a codebook. The difference between the original and approximated data and the codebook address are the compressed data that are needed for decompression (Pickering and Ryan 2006). Examples that use VQ for hyperspectral image compression are given by Ryan and Arnold (1997a) and Ryan and Arnold (1997b). VQ differs from the compression scheme, illustrated in Figure 2, since it encodes the data in one stage, covering both the spatial and the spectral domains. However, in the study by Pickering and Ryan (2000), DCT was applied in the spectral domain in order to compress the residual data produced by the mean-normalized VQ algorithm in the spatial domain, which may be seen as compliant with Figure 2.

In transform coding, the original hyperspectral data are multiplied by a set of *basis vectors* to produce a set of product values (Pickering and Ryan 2006). The basis vectors differ depending on the particular transform used, e.g. discrete wavelet transform (DWT), DCT, and KLT (also known as principal component analysis, PCA). Transform coding such as DWT and DCT can be used for either spectral or spatial decorrelation in hyperspectral compression (Baizert et al. 2001; Lee et al. 2002; Qian and Fowler 2007; Zhang et al. 2009). KLT, on the other hand, has been used for spectral decorrelation due to its intrinsic energy-compacting capability that is based on statistical method (Saghri et al. 1995; Blanes and Serra-Sagristà 2009), e.g. KLT for spectral and DCT for spatial decorrelation in Saghri et al. (1995), DWT for spectral and spatial decorrelation in Liu and Zhao (2008) and integerKLT for spectral and DWT for spatial decorrelation as in Blanes and Serra-Sagristà (2009).

Examples of coding standards that have been used widely in hyperspectral image compression are the Joint Photographic Experts Group (JPEG) and JPEG2000. JPEG has several modes, e.g. a baseline mode, which is lossy and based on DCT and a lossless mode, which uses a predictive algorithm. JPEG2000 (Part I) is based on DWT using the LeGall 5/3 filter for lossless compression and the Cohen–Daubechies–Feauveau (CDF) 9/7 filter for lossy compression (Santa-Cruz et al. 2000). In most applications of hyperspectral compression, these standards have been used for spatial decorrelation (Hunt and Rodriguez 2004; Penna et al. 2005; Mat Noor et al. 2010; Qian and Fowler 2007).

CCSDS has recently published a new recommended standard for lossless multispectral and hyperspectral image compression for space applications (CCSDS 2012b). It is based on a predictive coding method that depends on the values of nearby samples in the current spectral band (where the reference pixel $S_{z,y,x}$ is located) and P preceding spectral bands, where P a user-specified parameter. In each spectral band, a *local sum* of to produce the predictor output. Finally, the predictor output is coded using an entropy coder that is adaptively adjusted to adapt changes in the statistics of the mapped prediction residuals as defined in CCSDS (2012a). The algorithm provides spatial–spectral decorrelation in one stage.

In this article, we investigate lossless hyperspectral image compression using the integerKLT transform as a spectral decorrelator. Further background material on

hyperspectral data analysis and compression for remote sensing can be found in Richards (1993), Mather (2004), Borengasser et al. (2008a) and Lillesand et al. (2008).

3. Review of hyperspectral spaceborne missions

This section reviews all past, present, and planned future hyperspectral missions that were known at the time of writing this article. Hyperspectral missions were reviewed in several previous studies including airborne platforms (Buckingham et al. 2002; Shippert 2003; Buckingham and Staenz 2008; Guelman and Ortenberg 2009), the history of remote sensing, and instruments and data analysis (Schaeppman 2007; Schaeppman et al. 2009). To the best of the authors' knowledge, none of the existing literature sources discusses image compression techniques from such missions.

The main characteristics of the missions, ordered chronologically by launch date, are summarized in Table 1, which includes details about compression algorithms and payload data processing that were lacking in previous reviews. The first column of Table 1 specifies the satellite mission along with the hyperspectral instrument (in square brackets), its sensor type (e.g. filter, grating, prism, etc., in parentheses) and the respective literature sources. The next column covers the launch date and current status of the mission. Brief mission objectives and the scanning type (i.e. pushbroom (PB) or whiskbroom (WB)) are the content of the third and fourth columns, respectively. The total mass, payload mass and the category of the satellite according to Table 2 (Barnhart et al. 2009) are covered in the fifth column. Information related to payload data processing, such as the compression algorithm, processor and on-board memory, is given in the seventh to ninth columns. The payload imager specifications in terms of radiometric resolution, spectral range, spectral resolution, number of bands, and ground sampling distance (GSD) are covered in the 10th to 14th columns. Explanation of spectral resolution terms, such as spectral sampling or full width at half-maximum (FWHM) of an input is given in Borengasser et al. (2008b) and ITT (2010). The downlink speed for transmission of the payload data to the ground station is in the last column of the table. Unavailable information is denoted by NA in the table. Items requiring clarification are labelled with superscript upper case letters and are explained briefly at the bottom of the table. Detailed description of the hyperspectral image compression and processing available on board is provided in the rest of the section.

3.1 Hyperspectral missions in the 1990s

The Midcourse Space Experiment (MSX) mission, which was a military mission, flew the first hyperspectral imagers in space in 1996. It carried nine hyperspectral sensors, called Ultraviolet and Visible Imagers and Spectrographic Imager (UVISI). The data control system (DCS) could compress the 12 bits/pixel to 8 bits/pixel images using an image processor (ADSP 2100 from Analog Devices Inc., Norwood, MA, USA) and a military standard processor (MIL-STD-1750A). Two tape recorders each of size 54 Gb (gigabits) were employed to store the images. The data were dumped to ground at a rate of 25 Mb s⁻¹ (Huebschman 1996).

Although failing shortly after being launched, Lewis has been acknowledged and referred to as the first civilian hyperspectral mission by Willoughby et al. (1996) and Wander (2007). The mission was launched on 23 August 1997, lost contact on 26 August and was destroyed after the spacecraft re-entered the atmosphere on 28 September of the same year (Anderson et al. 1998). Data collection from the HSI imager and storage into a Solid State Recorder (SSR) were intended to take no more than 15 min of the 90 min orbital period. Images in the SSR could be compressed using the on-board computer (Willoughby et al. 1996).

Table 1. Hyperspectral image compression systems on board space missions.

Satellite/mission [sensor] (spectrometer type)	Launch date (Status)	Mission objectives	Scanning type	Mass (kg)		Category	Compression algorithms	Payload data processing	On- Board memory (Gbit)	Radiometric resolution (bits)	Spectral range (nm)	Spectral resolution (nm)	No. of bands	GSD (m)	Downlink speed(Mbps)
				Satellite	Payload										
1	2	3	4	5	6	7	8	9	10	11	12	13	14	15	
MSX [UVISI](filter wheel)(Stott et al. 1996; Heffernan et al. 1996; Skullney et al. 1996; Huebschman 1996)	24, April 1996(Retired in July 2008)	Military purposes	WB	2812	217	Large	NA	ADSP 2100& MIL-STD-1750A	108	12	110-900	0.5-4.3	272	100 - 800 (nadir at 900km alt.)	25
Lewis [HSI](filter)(Willoughby et al. 1996; Wander 2007; Marshall 1995)	23, August 1997(Failure after launched)	Earth observation & remote sensing	PB	385.6	NA	Mini	NA	NA	40	12-VNIR & SWIR	400-2500	5	384	30	0.4-274
Terra, Aqua [MODIS](filter)(Frazier 2010; Parkinson 2003; Xiong et al. 2006; Przyborski 2011)	18, December 1999(Terra) 4, May 2002 (Aqua)(Both running)	Land & ocean, snow & ice, temperature, clouds & land cover monitoring	WB	5190 (Terra),2934 (Aqua)	229	Large	NA	12-MHz MIL-STD 1750A	NA	12	410-14500	NA	36	250, 500, 1000	150 (Ku-band)
ARIES-1 [ARIES-1](NA)(Guelman and Ortenberg 2009; Merton and Huntington 1999) ^A	Planned-2000(Cancelled-March 2003)	Vegetation research	NA	<500	NA	Mini	NA	NA	NA	NA	400-1000 2000-2500 1000-2000	19 (FWHM) 15 (FWHM) 15 & 30 (FWHM)	32 32 32	30	NA
NEMO [COIS](grating)(Wilson and Baugh 1999; Vincent 1999; Fisher et al. 1998)	Planned-mid-2000(never flown)	DoD applications, land & water monitoring	PB	295	141 ^B	Mini	ORASIS	Parallel array of DSPs (2.5GFLOPS)	48	NA	400-2500	10	210	30, 60	150 - normal mode (X-band) 1 - tactical mode (S-band)

MightySat II.1 [FTHSI](Fourier Transform)(Barducci et al. 2006; Freeman et al. 2000; Yarbrough et al. 2002)	19, July 2000 (turned off in August 2002)	Air Force missions	PB	121	20	Mini	NA	DSP-Quad C40 (TMS320C40×4)	3	8/12	470-1050	85cm ⁻¹	256 28	1
--	--	--------------------	----	-----	----	------	----	----------------------------	---	------	----------	--------------------	--------	---

EO-1 [Hyperion] (grating) (eoPortal 2010; Pearlman et al. 2000; Pearlman et al. 2003; US_Geological_Survey 2011; Smith and Kessler 1999; Rabideau et al. 2006)	21, November 2000(Running)	Land imaging instrumentation	PB	572	49	Medium	Rice coding	RISC processor-Mongoose 5 (12MHz)	48	12	400-2500	≈10 (FWHM)	220	30	105 (X-band)
Orbview-4 [OHIS] (NA) (eoPortal 2010)	21, September 2001(Launch failure)	Earth observation for military & civilian	WB	368	NA	Mini	No compression	NA	32	12	400-2500	NA	200	8	150 (X-band)
PROBA-1 [CHRIS] (prism) (Cutter and Sweeting 2007; Bermyn 2000)	22, October 2001 (Running)	Multi-angle earth observation & aerosol properties of atmosphere	PB	94	14	Micro	NA	ADSP21020	1.2	12	400-1050	1.25-11.3	18, 62, 37	18/34	0.2 – 1 (S-band)
EnviSat [MERIS] (grating) (eoPortal 2010; Louet 2001; Bezy et al. 1999; Dubock et al. June 2001; ESA 2012)	1, March 2002(Ended on 8, April 2012)	Land & atmosphere monitoring	PB	8140	200	Large	NA	NA	150	12	390-1040	1.25 (spectral sampling)	15	300, 1200	50/100 (X-band)
Mars-Express [OMEGA] (grating) (ESA 2009; Melchiorri et al. 2006; Bonello et al. 2004; Bibring et al. 2004)	2, Jun2003(Running)	Mars surface exploration	Visible-PB IR-WB	1120	113 ^B	Large	Wavelet based compression	TSC21020 Temic Processor	12	NA	VNIR: 350-1050 SWIR-C: 930-2690 SWIR-L: 2520-5090	7.5 14 23	352	300	0.23
Aura [OMI& TES] (grating& Fourier Transform) (eoPortal 2010; Schoeberl et al. 2006; Wilson 2007; Tyler and Varanasi 2001)	15, July 2004(Running)	Climate & ozone monitoring	PB	2967	65 (OMI) 385(TES)	Large	NA	20 MIPS RISC Processor (TES)	100 (OMI)	NA	270-500 (OMI) 3200-15400 (TES)	0.42-0.63 (FWHM) (OMI) 0.025cm ⁻¹ (TES)	740 (OMI)	1300×2400 (nadir)(OMI)	155 (X-band)
Mars Reconnaissance Orbiter [CRISM] (grating) (Beisser 2011; Viotti 2008)	12, August 2005 (Running)	Mars exploration	PB	2180	32.92	Large	NA	NA	160	NA	VNIR: 362-1053 IR: 1002-3920	6.55 (spectral sampling)	545	20	6

(Continued)

Table 1. (Continued).

Satellite/mission [sensor] (spectrometer type)	Launch date (Status)	Mission objectives	Scanning type	Mass (kg)		Category	Compression algorithms	Payload data processing	On- Board memory(Gbit)	Radiometric resolution (bits)	Spectral range (nm)	Spectral resolution (nm)	No. of bands	GSD (m)	Downlink speed(Mb ps)
				Satellite	Payload										
1	2	3	4	5	6	7	8	9	10	11	12	13	14	15	
IMS-1/TWSat [HySI-T](wedge filter)(eoPortal 2010; Thyagarajan and Raghava Murthy 2009)	28, April 2008(Running)	Medium resolution imagery	PB	83	3.4	Micro	JPEG2000	NA	16	10	400-950	8 (spectral sampling)	64	550	8 (S-band)
TacSat-3 [ARTEMIS](grating)(eoPortal 2010; Davis and Straight 2006; Troxel et al. 2008b; Writers 2012)	19, May2009(Ended on 30, April 2012)	Military purposes	PB	400	170	Mini	NA	Xilinx field-programmable gate array (FPGA)	128	10	400-2500	5 (spectral sampling)	NA	NA	45/137/274
HERO [HERO](grating)(Bergeron et al. 2008; Bergeron et al. 2005) ^C	NA(In plan)	Vegetation, environment & health monitoring	PB	500	NA	Medium	Near-lossless Vector Quantization (VQ)	Xilinx FPGA (Real-Time) Virtex II (Non Real-Time)	1000	12	400-2500	~10 (FWHM)	210	30	150 (X-band – 2 channels)
PRISMA [PRISMA](prism)(eoPortal 2010; Galeazzi et al. 2008; Paolo et al. 2010; Sacchetti et al. 2009) ^P	2012(In plan)	Natural resources & atmosphere monitoring	PB	<500	<90	Mini	NA	NA	256	12	VNIR: 400-1010 SWIR: 920-2505	≤12	~240	30	155 (X-band)
TAIKI [HSC-III](grating)(Aoyanagi et al. 2010; Aoyanagi et al. 2011; eoPortal 2010) ^F	2012(In plan)	Agricultural monitoring	PB	50	10	Micro	NA	32-bit RISC	240	10	400-1000	10	138	15	10 (Ku-band)
EnMAP [HSI](prism)(Hofer et al. 2010; Stuffer et al. 2007))	2014(In plan)	Agriculture, forestry monitoring	PB	870	325	Medium	NA	NA	512	14	420-2450	5 VNIR 10 SWIR (spectral sampling)	228	30	320

HyspIRI [HyTES](grating)(Buckner 2008; Green et al. 2008; eoPortal 2010; Johnson et al. 2009; Hook et al. 2010; Hook 2011) ^F	2015 (In plan)	Land surface composition	PB	100	NA	Mini	NA	NA	NA	NA	7500-12000	17.6 (spectral sampling)	256	36.4 (20000 m alt.)	NA
HYPXIM [NA](prism) (Michel et al. 2010)	before 2018 (In plan)	Vegetation, geoscience, atmosphere, security & defence	PB	<195	60	Mini	Adaptive compression	NA	NA	NA	400-2500	10	210	15	150 (X-band)
-Challenging (2 satellite constellation) - Performance	before 2020 (In plan)		PB	<605	~100	Medium	Adaptive compression	NA	NA	NA	VNIR-SWIR: 400-2500 Thermal IR: 90-150	VNIR-SWIR: 10 Thermal IR: 90-150	VNIR- Thermal IR: 40	VNIR- Thermal IR: 8 100	270 (X-band)

Notes:

NA, Information not available; PB, Pushbroom; WB, Whiskbroom

^A Australian Resource Information and Environment Satellite-1 (ARIES-1)

^B The payload mass includes all the payloads of the mission.

^C Proposed satellite and sensor specification are discussed by Bergeron et al. (2008). Mission was initially targeted to be launched in 2009 but no further information as of the time of writing could be found.

^D Most of the latest information is from Paolo et al. (2010)

^E Techniques to overcome large data are proposed but compression algorithms are not mentioned.

^F Mission requirement are discussed by Green et al. (2008). Imager specifications for testing are given by Johnson et al. (2009), Hook et al. (2010), and Hook (2011). Prediction, KLT, wavelet & SPIHT algorithm are proposed by Buckner (2008)

Table 2. Satellite categories by mass.

Group name	Wet Mass (kg)	Large/Small Satellite
Large satellite	> 1000	Large satellite
Medium sized satellite	500 – 1000	
Mini satellite	100 – 500	Small satellite
Micro satellite	10 – 100	
Nano satellite	1 – 10	
Pico satellite	0.1 – 1	
Femto satellite	< 0.1	

The Terra mission was launched in 1999 and carried the Moderate Resolution Imaging Spectroradiometer (MODIS). MODIS was initially referred to as a non-hyperspectral sensor in Buckingham and Staenz (2008), but it has proven to be exceptionally useful for many applications and has since been categorized as a civilian hyperspectral sensor. A 12 MHz Military Standard (MIL-STD) 1750A processor was used to pack the hyperspectral data from all 36 bands using a CCSDS data packet format (Frazier 2010).

3.2 Hyperspectral missions during 2000 - 2005

The Aqua mission, launched in 2002, also carried a MODIS sensor. Both the Terra and Aqua missions are still nominally operational (eoPortal 2010), although a few of the payloads are not functional.

The Naval EarthMap Observer (NEMO) mission carrying a Coastal Ocean Imaging Spectrometer (COIS) sensor was planned for launch in 2000, but never flew. This mission used a custom compression algorithm called the Optical Real-Time Adaptive Signature Identification System (ORASIS) on a parallel array of 2.5 GFLOPs (Giga floating-point operations per second) DSPs. ORASIS offered automated and adaptive signature recognition capability for image analysis of military and commercial imagery (Wilson and Baugh 1999). The signature recognition algorithm analyses each spectral band sequentially, discarding duplicate bands and processing only the unique spectral band to map the required location in the scene (Vincent 1999). Convex set methods and orthogonal projection techniques are used for the image analysis, followed by the creation of matched filters to decode the image (Palmadesso et al. 1995; Bowles et al. 1996).

The MightySat II.1 satellite (2000–2002), carrying a Fourier Transform Hyperspectral Imager (FTHSI), is the first mission of its kind, encoding wavelength through an interferometer (Barducci et al. 2006). FTHSI shows the advantages of Fourier systems over dispersive hyperspectral imagers by recording the full spectra without any time delay and decoupling the spatial and spectral signatures (eoPortal 2010). A Quad C40 (QC40) processor comprising four TMS320C40 DSP chips was used for the payload processing (Barducci et al. 2006). Although no specific compression method has been reported, several algorithms for on-board processing have been implemented, such as apodization (improvement in the dynamic range of the image), spectral filtering, and fast Fourier transform (FFT). However, there were a few problems that rendered the on-board processing unrealistic and therefore the raw data were downloaded and processed on the ground (Barducci et al. 2006).

The Earth Observing 1 (EO-1) mission, launched in 2000 with Hyperion as its imaging spectrometer, is still operational (eoPortal 2010). After capturing ground images, the data are sent to the payload processing unit called Wideband Advanced Recorder and Processor (WARP) and are stored inside a memory board with a capacity of 24×2 Gb (Smith and

Kessler 1999). A processor board inside the WARP comprising a 32 bit, 12 MHz Reduced-Instruction-Set Computing (RISC) microprocessor, Mongoose 5, reads the images from the memory board and compresses them using the Rice algorithm (Rice and Plaunt 1971). The algorithm also reformats the data into Band Sequential (BSQ) format, one of the digital formats for storing a multi-spectral image in data memory, before sending it back to the memory boards (Smith and Kessler 1999). The image compression ratio achievable is 1.8 depending on image entropy.

The Orbview-4 mission, launched in 2001 and which carried the OrbView Hyperspectral Imaging System (OHIS), did not use any compression method for its hyperspectral data (eoPortal 2010). The mission was aborted due to a launch failure (Boucher 2001).

The Project for On-Board Autonomy 1 (PROBA-1) mission, launched in 2001, is a European Space Agency (ESA) hyperspectral mission based on a micro-satellite platform that is still operational (eoPortal 2010). PROBA-1 carries the Compact High Resolution Imaging Spectrometer (CHRIS) imager from Surrey Satellite Technology Ltd. (SSTL), Guildford, UK. It was reported that a compression algorithm for it was under active development (Read 2003). The imager's data processing unit (DPU), called payload processing unit, consists of a mass memory unit (MMU) for data storage (1 Gb), comprising a DSP (ADSP21020) for image processing during and post-acquisition (Bermyn 2000). The complete memory content can be dumped in at least two passes of about 10 min in 12 h, via downlink at tuneable data rates from 2 kb s^{-1} to 1 Mb s^{-1} (Bermyn 2000). (A pass refers to the satellite as seen from the ground station, for the duration of an active communications link.)

The ESA Environmental Satellite (EnviSat) mission (2002–2012) carried the Medium Resolution Imaging Spectrometer (MERIS) (eoPortal 2010). Buckingham and Staenz (2008) have referred to MERIS as a hyperspectral sensor by design, but the datasets received are not hyperspectral. No information about the on-board data compression algorithm is available. Images captured by MERIS are processed by a video electronic unit and a digital processing unit. Raw data are transmitted to the ground and corrected thereafter (Bezy et al. 1999).

Mars-Express, which was launched in 2003, is an interplanetary exploration mission that is aimed at visible and near-IR observation of the surface and atmosphere on Mars. According to Bibring et al. (2004), the hyperspectral imagery captured by the on-board imager, Observatoire pour la Minéralogie, l'Eau, les Glaces, et l'Activité (OMEGA), is compressed using a wavelet-based algorithm through its command and data processing unit (CDPU), followed by formatting of the processed data. The CDPU is based on a TSC21020 Temic processor with 6 MB static random-access memory (SRAM) compressing and formatting of the data into a 3-D-packaged highly miniaturized cube.

Aura is a mission launched in 2004 to monitor atmospheric and climatic changes using two hyperspectral imagers the ozone monitoring instrument (OMI) and the tropospheric emission spectrometer (TES), and is based on an IR-imaging Fourier Transform type of hyperspectral imager (Schoeberl et al. 2006). The command and data handling subsystem (C&DH) includes a 20 million instructions per second (MIPS) RISC processor with 128 MB of RAM, 3 MB of electrically erasable programmable read-only memory (EEPROM) and a Versa Module Europa (VME) interface to the instrument communication and control bus. C&DH has a high-rated data buffer and formats all science data into 8192-byte CCSDS telemetry packets (Tyler and Varanasi 2001).

Mars Reconnaissance is another Mars exploration mission, launched in 2005 to study the mineralogy and atmosphere of the red planet through its hyperspectral imager, the Compact Reconnaissance Imaging Spectrometer for Mars (CRISM). The DPCM method is used for lossless image compression (Murchie et al. 2007). Processing options, such as

offset subtraction, gain multiplication, and detector row selection can also be performed prior to compression. All image processing functions are supported by the processor system in the DPU. The processor system uses an Actel field-programmable gate array (FPGA) that also generates telemetry headers for image data before sending it to the spacecraft SSR for transmission to the Earth.

3.3 Hyperspectral missions since 2006

The Indian Microsatellite-1 (IMS-1), previously known as the Third World Satellite (TWSat), was launched in 2008. IMS-1 carries the hyperspectral imager HySI-T and is another example of a micro-satellite platform based mission. On-board image compression is performed using the JPEG2000 algorithm with a compression ratio of 3.4:1 (eoPortal 2010).

The Tactical Satellite-3 (TacSat-3) mission was launched in 2009 and was recently ended after the satellite was de-orbited and subsequently burned up in the Earth's atmosphere (Writers 2012). This mission represents the current state of the art in hyperspectral missions flown to date. The hyperspectral imager (HSI) payload houses the Advanced Responsive Tactically Effective Imaging Spectrometer (ARTEMIS), as well as a Responsive Avionics Reconfigurable Computer (RA-RCC) board and a G4-Single Board Computer (SBC) (Troxel et al. 2008a). The RA-RCC's primary functions are payload control and processing of the sensor data. The RA-RCC consists of four FPGAs including one Actel RTAX2000 and three Xilinx V4LX160 co-processors (COPs). The COP FPGAs enable the deployment of various high-performance signal-processing algorithms providing libraries of predefined functions allowing developers to build custom functionality as required. The compression algorithms used on board the satellite are not disclosed in the open literature; however, as such algorithms could easily be implemented, as discussed by Troxel et al. (2008b).

There are a number of hyperspectral missions that are at the planning stage, but very few details are available about compression methods to be incorporated into their imaging payload systems. It is suggested that the Hyperspectral Environment and Resource Observer (HERO) mission will use a VQ compression method implemented on an FPGA to support real-time and non-real-time operations (Bergeron et al. 2005) and the HYPXIM mission will utilize an adaptive compression method (Michel et al. 2010), but no specific methods are disclosed. No information regarding image compression on board the future missions PRISMA (PRecursore Iper Spettrale della Missione Operativa), TAIKI (meaning 'big tree' in Japanese), EnMAP (Environmental Mapping and Analysis Program) and HypIRI (Hyperspectral Infrared Imager) was found in the available literature at the time of writing this article.

Table 3 lists the hyperspectral missions that have data compression capabilities on board, according to the literature. The need for on-board compression of hyperspectral imagery will grow in the future due to the even greater amount of valuable data that will be generated by the next generation of instruments.

Table 3. On-board hyperspectral image compression

Mission	Launched	Status	Compression Scheme
EO-1	2000	Running	Rice coding
Mars-Express	2003	Running	Wavelet-based compression
IMS-1	2008	Running	JPEG2000
NEMO		Cancelled	Custom compression
HYPXIM		Planned	Adaptive compression
HERO		Planned	Vector quantization

4. The integer Karhunen-Loève transform

The KLT has been used as a lossy spectral decorrelator to reduce spectral redundancy in multi-component image compression studies (e.g. hyperspectral imaging for remote sensing and magnetic resonance imaging (MRI) for medical applications (Yodchanan 2008)). KLT has also been applied to facial recognition (Nefian and Hayes 1998) and pattern finding in high-dimension data Quintiliano and Santa-Rosa (2003).

When using KLT to encode a multi-component image (e.g. a hyperspectral image with N spectral bands), an $N \times N$ eigenvector matrix is generated called the KLT transform matrix. KLT is also known as principal component analysis (PCA). In PCA, a number, P , of principal components (PCs) are selected and sorted according to the eigenvalue, resulting in the eigenvector matrix $P \times N$. When all PCs are retained (i.e. an $N \times N$ eigenvector matrix is generated), the PCA transform coding is referred to as KLT (Qian and Fowler 2007). In other words, spectral decorrelation using KLT is equivalent to PCA, in which the number of PCs is equal to the number of spectral bands.

Due to the arrangement of PCs by eigenvalue, KLT is said to have *energy compaction* capability which is evidenced by the fact that the main details of the encoded image are visible in the first few eigen planes (spectral bands of the encoded image) followed by the remaining planes that do not have visible features. The remaining planes can be coarsely quantized (Saghri et al. 1995) and sometimes can even be dropped to increase the signal-to-noise ratio (SNR) (Qian and Fowler 2007). This is the reason why KLT is the optimal method to reduce spectral redundancy or, in other words, similarity between bands. KLT has proven to be the most efficient spectral decorrelator compared with the DCT (Saghri et al. 1995) and the DWT (Qian and Fowler 2007).

The output from KLT, however, is non-reversible since it consists of floating-point numbers and rounding is necessary, which leads to a lossy transformation. An approximation of KLT was proposed by Hao and Shi (2003) that is based on matrix factorization proposed in Hao and Shi (2001), representing the output in an integer form, hence it was called 'Integer KLT'. As in the original KLT transform, the compression of a hyperspectral image with N number of bands will involve generating an eigenvector matrix \mathbf{A} of size $N \times N$ from the covariance matrix between each pair of bands. Matrix factorization will be applied on the \mathbf{A} matrix, which is a non-singular (i.e. $\det(\mathbf{A}) = |1|$) matrix into four $N \times N$ matrices: a permutation matrix, \mathbf{P} , and three other matrices called *triangular elementary reversible matrices* (TERMs): \mathbf{L} (lower TERM), \mathbf{U} (upper TERM), and \mathbf{S} (lower TERM). The factorization is not unique and depends on the pivoting method used that will affect the error between the integer approximation and the original KLT transformation (Lei et al. 2009). The intrinsic energy-compacting capability of KLT will be affected by the factorization, so the error should be minimized as much as possible.

The integer KLT has the same characteristics as KLT except that it is reversible and therefore can be used for progressive lossy-to-lossless multi-component compression. Original and encoded images (grey level) for selected bands of the AVIRIS Low Altitude Scene 1 are shown in Figure 3 and 4, respectively. By comparing the original and the encoded images, it can be seen that a significant portion of the detail is contained in the early eigen planes (shown as eigen planes 1, 5, and 10), which decreases towards the end (as in eigen planes 35, 40, and 45). Currently, there are no satellite missions that use a KLT-based method for hyperspectral compression on board.

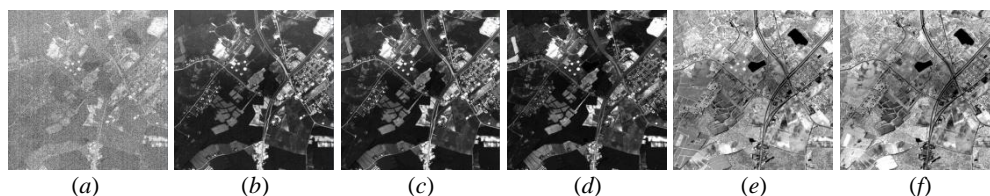


Figure 3. Original Low Altitude Scene 1 AVIRIS image from (a) spectral band 1, (b) spectral band 5, (c) spectral band 10, (d) spectral band 35, (e) spectral band 40, and (f) spectral band 45.

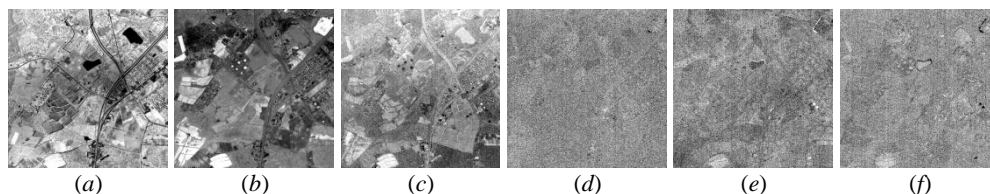


Figure 4. Encoded Low Altitude Scene 1 AVIRIS image using integer KLT from (a) eigenplane 1, (b) eigenplane 5, (c) eigen plane 10, (d) eigenplane 35, (e) eigenplane 40, and (f) eigenplane 45.

4.1 Integer KLT as a lossless spectral decorrelator

Partial pivoting as part of integer KLT was introduced by Hao and Shi (2001), and several studies focused on different types of pivoting (Galli and Salzo 2004; Xin et al. 2007a, 2007b). *Quasi-complete* pivoting (Galli and Salzo 2004) was reported as the best method to minimize the integer approximation error by Blanes and Serra-Sagrìstà (2009) and Lei et al. (2009) and was used by Jing et al. (2008) and Yodchanan (2008). The integer KLT with *quasi-complete* pivoting was compared with the linear prediction and band differential methods to investigate the decorrelation performance, and it was shown that the integer KLT yields the highest compression ratio when combined with lossless JPEG2000 (Mat Noor et al. 2010).

Here we present new experimental results comparing the integer KLT with another spectral decorrelation method, namely the multi-component compression algorithm in Part II of the JPEG2000 Standard. Table 4 shows the performance of the integer KLT with

Table 4. Performance comparison of the integer KLT and JPEG2000 algorithms.

Hyperspectral Images	Multi-component JPEG2K	Integer KLT+JPEG2K	Improvement (%)
Cuprite Scene 1	2.9362	3.2002	8.99
Cuprite Scene 3	2.9174	3.1772	8.91
Jasper Scene 1	2.8046	3.2113	14.50
Jasper Scene 3	2.7732	3.2052	15.58
Low Altitude Scene 1	2.6149	3.0001	14.73
Low Altitude Scene 2	2.5860	2.9849	15.43
Yellowstone Calibrated Scene 0	3.2222	4.0101	24.45
Yellowstone Calibrated Scene 3	3.2980	4.1036	24.43
Yellowstone Calibrated Scene 10	4.1959	4.6296	10.34
Yellowstone Calibrated Scene 11	3.6306	4.2661	17.50
Yellowstone Calibrated Scene 18	3.2690	4.0546	24.03
Maine Non-Calibrated Scene 10	3.3517	3.8303	14.28
Hawaii Non-Calibrated Scene 1	3.4958	4.0151	14.85

quasi-complete pivoting and the multi-component JPEG2000 (MC-JPEG2K) algorithm for 13 AVIRIS images (NASA-JPL 2010a, 2010b). The performance is evaluated in terms of the overall compression ratio where the lossless JPEG2000 (JPEG2K) algorithm is used for spatial compression. As can be seen from Table 4, the integer KLT brings an average improvement of 16%, which corroborates the previous findings of Mat Noor et al. (2010).

The KLT algorithm is very computationally intensive and its approximation, the integer KLT, has even higher complexity due to the additional operations (i.e. matrix factorization). A low-complexity multiplierless reversible KLT was proposed by Lei et al. (2009) based on the method suggested in Penna et al. (2006). A 3-D medical image with a spatial size of $M \times N$ pixels is sampled into the matrix $M' \times N'$ ($M' \leq M$ and $N' \leq N$), which is used to compute the covariance matrix and the factorization stage. Using a sampling factor $\rho = M' \times N' / M \times N = 0.01$, the three floating-point TERM matrices of the factorization stage are quantized into fractions with a denominator value equal to a power of 2. The integer KLT is then realized through shifts and additions without a multiplication. The proposed scheme achieves around 12% improvement in terms of execution time as compared to the case where $\rho = 1$ and floating-point TERM matrices were used.

The integer KLT is suitable for hyperspectral missions that require lossless compression with high performance as shown above. Even though it is complex due to the covariance matrix calculation and factorization process, low-complexity schemes can improve its execution time. Remote sensing applications such as military reconnaissance, vegetation studies and natural resources monitoring could benefit from the lossless nature of the algorithm.

4.2 Clustering and tiling techniques for integer KLT

Clustering and tiling techniques can be used in conjunction with the integer KLT algorithm. These approaches will not affect the losslessness of the algorithm.

Clustering of integer KLT can be performed by encoding a group of n bands rather than the total number of bands N in a hyperspectral image, where $n \leq N$. To encode all of the bands, the process is repeated for c iterations, where $c = N/n$ is the number of clusters. Clustering of the integer KLT transform was performed through multilevel approaches (Yodchanan et al. 2006a; Yodchanan et al. 2006b; Yodchanan 2008; Blanes and Serra-Sagristà 2009). Blanes and Serra-Sagristà (2009) found that the multilevel, clustered version of the integer KLT could bring some degree of spectral scalability for lossy-to-lossless coding in comparison with the normal clustering approach.

Figure 5 (Blanes and Serra-Sagristà 2009) shows a block diagram of normal and multilevel clustering. Multilevel clustering is a stacked version of the normal clustering performed on the higher energy components. The next level is derived from the previous levels until only one cluster is processed at the highest level. Introducing clustering in integer KLT reduces the memory usage, which is especially useful in embedded applications with constrained memory resources. Multilevel clustering process costs $(2 - 1/c)$ times the cost of a normal clustering and makes the algorithm slightly more complex.

In the case of a large spatial size of satellite images, tiling is applied before performing any kind of image processing (Yu et al. 2009). Tiling can also constrain error propagation to the smaller area of the tile rather than the whole spatial size of the original image. The introduction of tiling in compression of satellite images has been proved to increase the resilience of the image compression algorithm to single-event upsets (SEUs) induced by

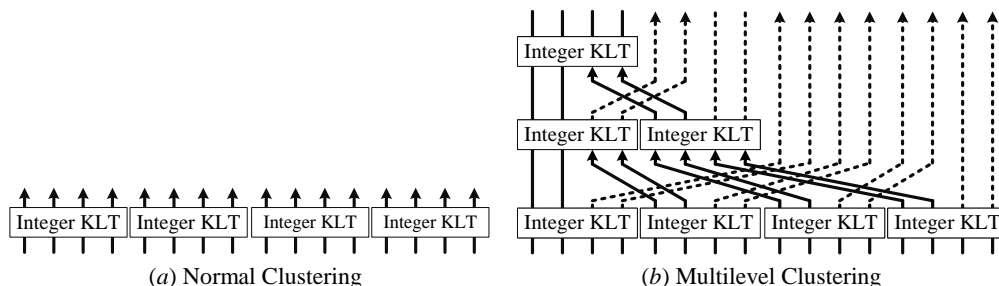


Figure 5. Clustering strategies.

radiation (Vladimirova and Steffens 2005; Vladimirova et al. 2006). However, the compression performance suffers if the tile size is too small. On the other hand, the tile size also determines the buffer size for the on-board storage, so it cannot be very large either (Mat Noor and Vladimirova 2011). A careful trade-off analysis is required to determine the right tile size.

5. Integer KLT modelling

In this section the integer KLT algorithm is characterised in terms of compression performance and latency. For the purpose of the integer KLT modelling, the algorithm was coded in C++ using previously developed Matlab code (Mat Noor et al. 2010; Mat Noor and Vladimirova 2011). This code was developed under the Visual Studio 2010 Ultimate Win32 project. The open source mathematical library ALGLIB (Bochkanov 2011) was employed for eigenvector calculation. The code was executed on a desktop computer with Intel® Core™ i7 880 processor at 3.06 GHz, 16 GB of RAM and Windows 7 x64 Enterprise as the operating system. The JPEG2000 algorithm implementation of Kakadu V 6.3 (Taubman 2010) was used for the lossless spectral and spatial decorrelation. The compression ratio (original size/compressed size) was evaluated inclusive of the four matrices (\mathbf{P} , \mathbf{L} , \mathbf{U} and \mathbf{S}).

5.1 Experiment Outline

Four hyperspectral images acquired from each of two hyperspectral sensors – the airborne AVIRIS (NASA-JPL 2010a, 2010b) and the spaceborne EO-1 Hyperion (USGS 2011) imager – are employed as the test images in this modelling study. AVIRIS images are taken at the nominal altitude of 20 km (Green et al. 1998). The choice of AVIRIS is motivated by the fact that its datasets have been used widely in hyperspectral image compression research, providing a good basis for comparison (Penna et al. 2006; Zhou et al. 2006; Kiely and Klimesh 2009). AVIRIS data have also been used for simulation of spaceborne imagery (Abrams 1992; Kalman and Pelzer 1993; Willart Soufflet and Santer 1993; Wetzel 1995). Hyperion is one of a few spaceborne hyperspectral imagers that are operational at the time of writing, and its imagery is employed to investigate integer KLT usability for implementation on board satellites. Hyperion is flown on the EO-1 satellite at 705 km altitude (Ungar et al. 2003).

The AVIRIS and Hyperion test images are listed in Table 5, which includes the abbreviated names used in this article and the acquisition details. All AVIRIS images were cropped spatially to a size of 512×512 pixels from the upper left corner for all 224 bands. The false-colour representations of these datasets are shown in Figure 6(a)-(d). All Hyperion images were cropped to a size of 256×256. Out of 242 bands, only 196 bands,

Table 5. AVIRIS and Hyperion datasets.

Imager/Sensor	Datasets	Abbreviation	Acquisition
AVIRIS	Jasper Ridge Scene 3	Jasper3	1997 datasets (NASA-JPL 2010b)
	Low Altitude Scene 2	Low2	"
	Yellowstone Calibrated Scene 11	YellowstoneCal11	2006 datasets (NASA-JPL 2010a)
	Yellowstone Calibrated Scene 18	YellowstoneCal18	"
Hyperion	EO1H0090112001140111PP_PF1_01	Greenland	20, May 2001
	EO1H0120312001129111P1_PF1_01	Boston	9, May 2001
	EO1H0140362001127110PP_AGS_01	Edenton(image of Northeastern Regional Airport, Edenton)	7, May 2001
	EO1H0150332001134111P1_AGS_01	Portobago(image of Portobago Bay)	14, May 2001

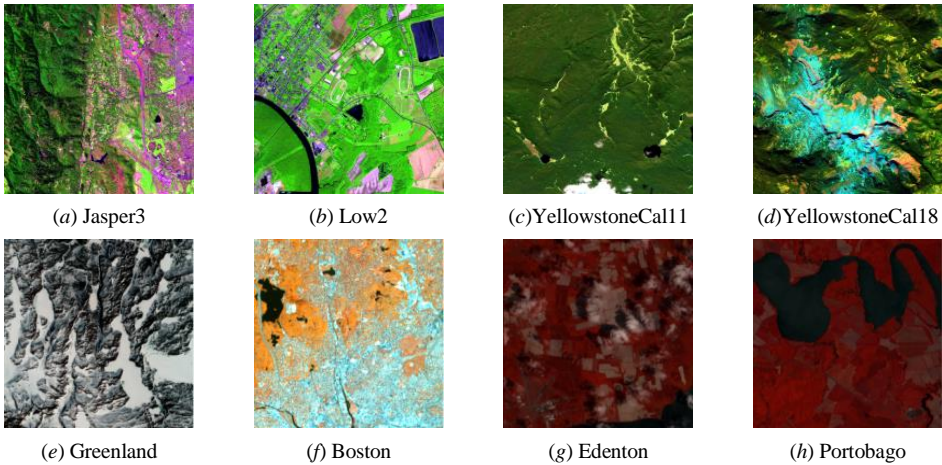


Figure 6. False-color representation for AVIRIS ((a)-(d)) and Hyperion ((e)-(h)) datasets.

which were classified as unique and calibrated, have been extracted (i.e. bands 8-57 and bands 79-224). False-colour representations of the images are shown in Figure 6(e)-(h).

In this work, only the normal clustering approach is applied due to focusing on lossless compression. Ten different numbers of clusters, c , are employed for the AVIRIS images: 1, 2, 4, 7, 8, 14, 16, 28, 32 and 56 and seven for the Hyperion images: 1, 2, 4, 7, 14, 28, and 49. When $c = 1$, the integer KLT is performed without a clustering. Four tile sizes are targeted for AVIRIS: 64×64 , 128×128 , 256×256 and 512×512 and three tile sizes for Hyperion: 64×64 , 128×128 and 256×256 . Comparison with a second spectral decorrelation method – the multi-component transform of JPEG2000 Part II – is carried out. The overall block diagram for this modelling experiment is presented in Figure 7.

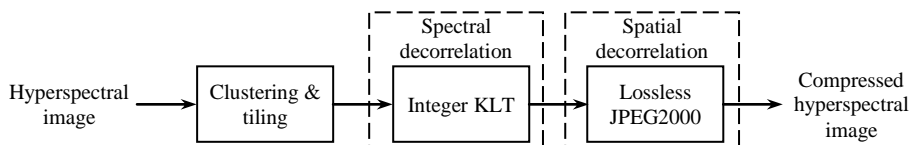


Figure 7. Lossless hyperspectral image compression for on-board application.

5.2 Compression performance analysis

Table 6 shows the compression ratio results achieved by modelling the compression scheme illustrated in Figure 7 for the AVIRIS test images. The combined integer KLT and JPEG2000 (IntKLT+JPEG2K) compression model is applied to four different tile sizes. Similarly, Table 7 shows the IntKLT+JPEG2K compression performance for the Hyperion test images at three tile sizes. Each column in Table 6 and 7 represents the compression ratio for a particular number of clusters, c . The highest compression ratio values, achieved for each image, tile and size are shaded in grey.

Figure 8 represents graphically the relationship between ratio, tile and cluster sizes for the AVIRIS performance data in Table 6, where the highest compression values are marked by circles in the graphs. The graphical representation of the data for the Hyperion images in Table 7 shows the same behaviour pattern, as that illustrated in Figure 8, despite the different nature of the image sources. As it can be seen from Figure 8, the highest compression ratio occurs in cases when clustering was performed (i.e. at $c > 1$), suggesting that clustering could increase the compression performance. It can also be seen clearly in Figure 8 that an overly large number of clusters, c (i.e. performing the operations on a small number of bands) negatively affects the compression ratio (Saghri et al. 1995). By observing the results across different tile sizes for each image in Figure 8 and Table 6 and 7, it can be concluded that a smaller tile size could definitely result in poorer compression performance, which is in agreement with Salomon (2007). However, from the point of view of algorithm robustness, the smaller tiling size is beneficial with regard to constraining error propagation, as discussed in Section 4.2.

For comparison purposes the multi-component transform of JPEG2000 Part II (MC-JPEG2K), combined with the spatial JPEG2000 transform, was also applied to the test images following a similar approach to the foregoing in terms of clustering and tiling. The MC-JPEG2K method utilizes the integer CDF 5/3 wavelet for the spectral decorrelation process. The modelling results obtained for the MC-JPEG2K based scheme showed the same pattern as that represented in Figure 8; however, in terms of compression performance the method lagged behind integer KLT. This can clearly be seen from Table 8, which presents the highest compression ratio values obtained using the IntKLT+JPEG2K and MC-JPEG2K algorithms and the corresponding number of clusters c as well as the improvement achieved by the integer KLT for the test images at all the tile sizes. The average improvement is around 9%, increasing with tile size within a 6% margin.

Comparing the performance results for the two datasets in Table 6-8, it will be noted that the airborne images have a higher compression ratio than the spaceborne images. The AVIRIS average highest compression ratios (shaded cells) for the AVIRIS images (Table 6 and 7) are higher than those for Hyperion by 25%, 30% and 33% at tile sizes 64×64 , 128×128 and 256×256 , respectively. Similarly, the performance improvement achieved by integer KLT over MC-JPEG2K for the AVIRIS images is on average higher than that for the Hyperion datasets by 2.19%, 7.05% and 10.23% at the tile size 64×64 , 128×128 and 256×256 , respectively. The different compression performance of the two types of hyperspectral images is due to a number of factors, including the distinctive nature of the imagers, etc.

Table 6. IntKLT+JPEG2K compression ratio for AVIRIS (airborne) datasets with clustering and tiling.

Tile Size	No. of clusters, c (No. of bands/cluster)	1 (224)	2 (112)	4 (56)	7 (32)	8 (28)	14 (16)	16 (14)	28 (8)	32 (7)	56 (4)
64×64	Jasper3	1.001	1.516	2.030	2.360	2.416	2.607	2.627	2.678	2.666	2.586
	Low2	0.979	1.467	1.944	2.243	2.298	2.470	2.491	2.541	2.533	2.468
	YellowstoneCal11	1.085	1.723	2.425	2.911	3.003	3.301	3.342	3.423	3.407	3.280
	YellowstoneCal18	1.070	1.686	2.346	2.791	2.867	3.125	3.151	3.190	3.166	3.006
128×128	Jasper3	2.108	2.559	2.844	2.961	2.968	2.994	2.978	2.923	2.889	2.743
	Low2	2.011	2.419	2.676	2.778	2.790	2.814	2.803	2.759	2.733	2.609
	YellowstoneCal11	2.522	3.210	3.675	3.872	3.892	3.932	3.920	3.821	3.767	3.527
	YellowstoneCal18	2.443	3.079	3.494	3.659	3.664	3.686	3.659	3.531	3.475	3.212
256×256	Jasper3	2.910	3.086	3.156	3.158	3.143	3.105	3.077	2.988	2.948	2.783
	Low2	2.724	2.881	2.950	2.952	2.946	2.913	2.892	2.818	2.787	2.647
	YellowstoneCal11	3.765	4.075	4.197	4.199	4.177	4.099	4.069	3.909	3.840	3.572
	YellowstoneCal18	3.587	3.868	3.965	3.955	3.924	3.847	3.800	3.616	3.553	3.260
512×512	Jasper3	3.205	3.244	3.237	3.205	3.181	3.128	3.096	3.000	2.958	2.789
	Low2	2.985	3.022	3.025	2.996	2.986	2.939	2.913	2.833	2.801	2.656
	YellowstoneCal11	4.266	4.339	4.325	4.249	4.216	4.106	4.067	3.897	3.822	3.557
	YellowstoneCal18	4.055	4.126	4.093	4.032	3.985	3.883	3.834	3.630	3.568	3.268

Table 7. IntKLT+JPEG2K compression ratio for Hyperion (spaceborne) datasets with clustering and tiling.

Tile Size	No. of clusters, c (No. of bands/cluster)	1 (196)	2 (98)	4 (49)	7 (28)	14 (14)	28 (7)	49 (4)
64×64	Greenland	0.993	1.411	1.784	1.998	2.154	2.190	2.169
	Boston	0.997	1.420	1.796	2.015	2.175	2.217	2.199
	Edenton	0.991	1.406	1.776	1.991	2.152	2.199	2.186
	Portobago	1.000	1.425	1.808	2.035	2.210	2.269	2.271
128×128	Greenland	1.785	2.061	2.228	2.289	2.313	2.270	2.213
	Boston	1.800	2.078	2.245	2.309	2.333	2.295	2.241
	Edenton	1.777	2.048	2.215	2.278	2.309	2.278	2.229
	Portobago	1.807	2.090	2.266	2.339	2.380	2.356	2.321
256×256	Greenland	2.224	2.323	2.368	2.370	2.353	2.288	2.222
	Boston	2.243	2.336	2.378	2.375	2.351	2.294	2.230
	Edenton	2.208	2.301	2.342	2.346	2.329	2.279	2.221
	Portobago	2.261	2.364	2.413	2.426	2.423	2.377	2.333

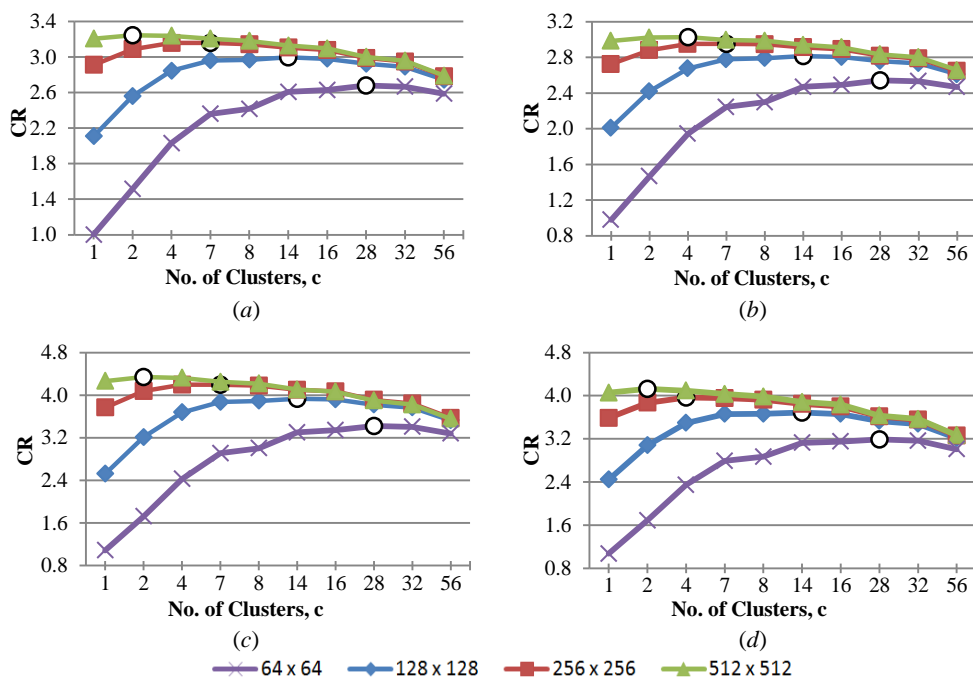


Figure 8. IntKLT+JPEG2000 compression ratio performance at different no. of clusters c and tile sizes for (a) Jasper3, (b) Low2, (c) YellowstoneCal11, and (d) YellowstoneCal18.

5.3 Compression latency analysis

In this analysis the execution time for the integer KLT compression process is measured without taking into account the input/output (I/O) time for the read/write operations from/to memory. In addition, the execution time accounts only for the integer KLT algorithm and does not include the time for performing spatial compression by Kakadu software.

Table 8. Comparison of maximum compression ratio for IntKLT+JPEG2K and MC-JPEG2K with clustering and tiling.

Tile size	Hyperspectral images	MC-JPEG2K		IntKLT+JPEG2000		Improvement (%)
		Compression ratio	No. of clusters c (bands/cluster)	Compression ratio	No. of clusters c (bands/cluster)	
64×64	Jasper3	2.4276	28 (8)	2.678	28 (8)	10.31
	Low2	2.2943	32 (7)	2.541	28 (8)	10.75
	YellowstoneCal11	3.0604	28 (8)	3.423	28 (8)	11.85
	YellowstoneCal18	2.7764	28 (8)	3.190	28 (8)	14.90
	Greenland	1.9774	28 (7)	2.190	28 (7)	10.75
	Boston	2.0202	28 (7)	2.217	28 (7)	9.74
	Edenton	2.0144	28 (7)	2.199	28 (7)	9.16
	Portobago	2.0758	28 (7)	2.271	49 (4)	9.40
128×128	Jasper3	2.6785	14 (16)	2.994	14 (16)	11.78
	Low2	2.5119	16 (14)	2.814	14 (16)	12.03
	YellowstoneCal11	3.4733	16 (14)	3.932	14 (16)	13.21
	YellowstoneCal18	3.1240	14 (16)	3.686	14 (16)	17.99
	Greenland	2.1463	14 (14)	2.313	14 (14)	7.77
	Boston	2.1875	14 (14)	2.333	14 (14)	6.65
	Edenton	2.1746	14 (14)	2.309	14 (14)	6.18
	Portobago	2.2407	14 (14)	2.380	14 (14)	6.22
256×256	Jasper3	2.7776	7 (32)	3.158	7 (32)	13.70
	Low2	2.5979	8 (28)	2.952	7 (32)	13.63
	YellowstoneCal11	3.6412	8 (28)	4.199	7 (32)	15.32
	YellowstoneCal18	3.2597	8 (28)	3.965	4 (56)	21.64
	Greenland	2.2096	7 (28)	2.370	7 (28)	7.26
	Boston	2.2472	7 (28)	2.378	4 (49)	5.82
	Edenton	2.2361	7 (28)	2.346	7 (28)	4.91
	Portobago	2.3017	14 (14)	2.426	7 (28)	5.40
512×512	Jasper3	2.8206	7 (32)	3.244	2 (112)	15.01
	Low2	2.6313	8 (28)	3.025	4 (56)	14.96
	YellowstoneCal11	3.7072	8 (28)	4.339	2 (112)	17.04
	YellowstoneCal18	3.3129	7 (32)	4.126	2 (112)	24.54

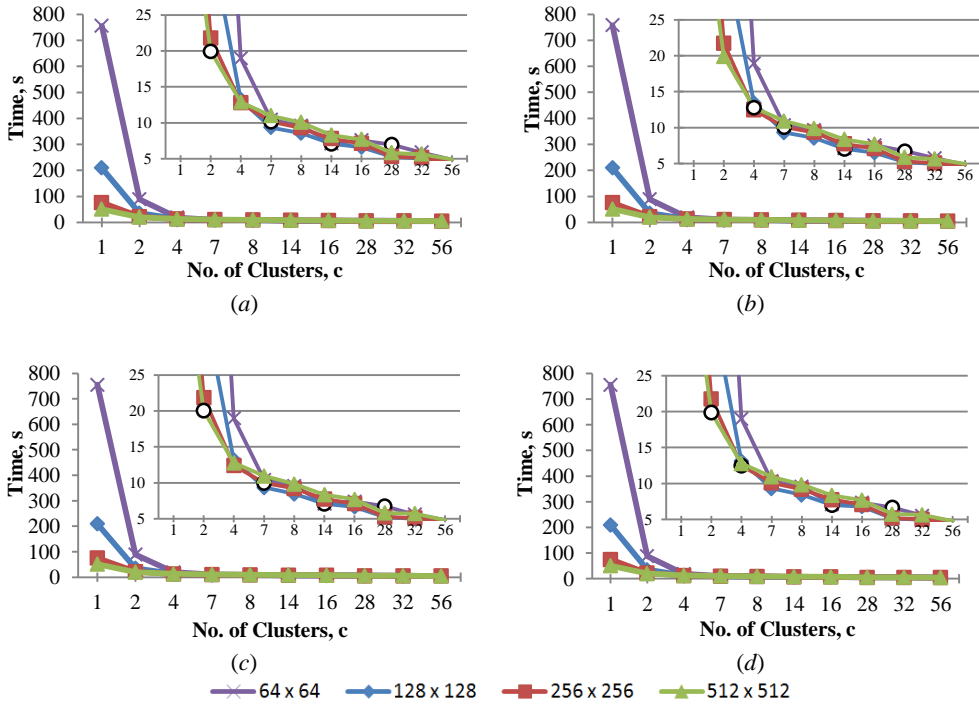
Table 9 and 10 show the execution time recorded for performing integer KLT on AVIRIS and Hyperion datasets, respectively, at tile sizes defined in Section 5.1. Each of the time measurements was repeated five times and the average value was calculated. Each column in the tables represents the execution time for a different number of clusters, c . Shaded in grey are the latency values corresponding to the highest compression ratios in Table 6 and 7. The execution times for AVIRIS images are then represented graphically in Figure 9. The execution time for the Hyperion images showed the same pattern as that of the AVIRIS images, and therefore it is not visualized. The smaller graphs within the main graphs in Figure 9 show the detailed behaviour between 5 and 25 seconds, where the circles mark the highest compression ratio values. It can be seen from Figure 9 that the fastest execution time is achieved by the largest number of clusters $c = 56$, although it does not yield the best compression ratio.

Table 9. Integer KLT execution time (seconds) on desktop computer for AVIRIS (airborne) datasets with clustering and tiling.

Tile Size	No. of clusters, c (No. of bands/cluster)	1 (224)	2 (112)	4 (56)	7 (32)	8 (28)	14 (16)	16 (14)	28 (8)	32 (7)	56 (4)
64×64	Jasper3	755.849	88.607	18.961	10.422	9.585	7.139	7.564	6.963	5.859	4.874
	Low2	757.987	88.448	18.927	10.321	9.648	7.141	7.534	6.723	5.756	4.845
	YellowstoneCal11	755.517	88.763	18.999	10.415	9.571	7.125	7.391	6.731	5.599	4.835
	YellowstoneCal18	755.437	88.408	19.020	10.308	9.558	7.138	7.343	6.659	5.526	4.761
128×128	Jasper3	209.412	35.261	13.196	9.346	8.560	7.103	6.603	5.289	5.059	4.549
	Low2	209.485	34.879	13.447	9.311	8.560	7.064	6.517	5.186	4.984	4.511
	YellowstoneCal11	209.520	34.979	13.179	9.358	8.464	7.091	6.673	5.243	5.025	4.492
	YellowstoneCal18	209.656	35.063	13.119	9.314	8.424	7.019	6.796	5.145	4.946	4.442
256×256	Jasper3	75.675	21.770	12.755	10.152	9.295	7.776	7.123	5.319	5.151	4.623
	Low2	75.404	21.737	12.462	10.067	9.332	7.728	7.097	5.265	5.092	4.614
	YellowstoneCal11	74.918	21.855	12.417	9.990	9.217	7.760	7.110	5.269	5.107	4.534
	YellowstoneCal18	74.875	21.750	12.488	10.100	9.201	7.757	7.057	5.201	5.020	4.535
512×512	Jasper3	50.610	19.937	12.894	10.972	10.054	8.291	7.690	5.827	5.636	4.907
	Low2	51.169	19.909	12.776	10.922	9.873	8.359	7.716	5.859	5.645	4.952
	YellowstoneCal11	51.003	20.061	12.779	10.966	9.857	8.365	7.704	5.818	5.725	4.846
	YellowstoneCal18	50.773	19.863	12.791	10.941	9.857	8.365	7.683	5.764	5.637	4.806

Table 10. Integer KLT execution time (seconds) on desktop computer for Hyperion (spaceborne) datasets with clustering and tiling.

Tile Size	No. of clusters, c (No. of bands/cluster)	1 (196)	2 (98)	4 (49)	7 (28)	14 (14)	28 (7)	49 (4)
64×64	Greenland	83.491	13.009	3.339	1.934	1.516	1.154	1.110
	Boston	83.236	13.133	3.323	1.981	1.528	1.146	1.067
	Edenton	82.733	13.120	3.323	1.963	1.524	1.106	1.083
	Portobago	83.646	13.135	3.354	2.075	1.419	1.095	1.035
128×128	Greenland	25.022	5.898	2.745	1.778	1.420	0.982	1.888
	Boston	25.054	5.776	2.666	1.810	1.356	1.060	2.013
	Edenton	25.040	5.832	2.605	1.761	1.451	1.031	2.061
	Portobago	25.053	5.784	2.715	1.762	1.450	1.029	1.997
256×256	Greenland	10.671	4.087	2.605	1.934	1.498	1.090	0.966
	Boston	10.842	4.088	2.590	1.904	1.451	1.076	0.968
	Edenton	10.827	4.087	2.620	1.871	1.449	1.045	0.971
	Portobago	10.701	4.071	2.606	1.889	1.466	1.093	0.966

Figure 9. Execution time at different no. of clusters c and tile sizes for (a) Jasper3, (b) Low2, (c) YellowstoneCal11, and (d) YellowstoneCal18.

The results clearly show that clustering can significantly improve latency. The reason for this may be that a larger number of clusters (i.e. a smaller number of bands to process) leads to a lower memory usage. However, the number of clusters must be selected based on

a trade-off between latency and performance as the compression ratio is lower when too few bands per cluster are to be decorrelated.

It can also be observed from Figure 9 that the introduction of tiling does not affect latency performance significantly. This is mainly because the number of bands in a hyperspectral image is the main factor that will determine the size of the eigenvector matrix, \mathbf{A} , in integer KLT, which will be used for factorization. However, at a smaller tile size, when $c = 1$ and 2, latency results are poor. This might be because ratio between the spectral and spatial components is too high for the AVIRIS and Hyperion datasets in the case when $c = 1$, especially for tile sizes of 64×64 and 128×128 pixels.

It can be seen from Table 9 and 10 that the Hyperion images are processed more rapidly, taking an average of 1.11 s at the highest compression ratios (shaded cell) compared with 6.77 s for the AVIRIS images at the 64×64 tile size. Similarly, the Hyperion datasets are encoded 5.65 and 8.60 s faster than the AVIRIS images at tile sizes of 128×128 and 256×256 , respectively. These differences are due to the fact that the 2D size of the AVIRIS datasets is four times larger than Hyperion (512×512 for AVIRIS and 256×256 for Hyperion) and in addition it has 28 more bands.

6. Integer KLT prototyping

This section is concerned with the implementation of integer KLT on an embedded hardware platform for rapid prototyping purposes. The integer KLT algorithm and software used for spatial compression were the same as those used in the desktop modelling described in Section 5. However, the implementation was somewhat restricted in terms of the clustering technique due to memory limitations.

The platform is the DSP development system from Texas Instruments (TI), OMAP-L137 EVM, which is based on the TI dual-core processor OMAP-L137, comprising the C6747 DSP and ARM9 processor cores, both running at up to 300 MHz. The software is developed in the C programming language using the Code Composer Studio V3.3 with DSP/BIOS V5.41 as its real-time kernel. It comes with a compiler that is specifically tuned to maximize the performance of the executable code. Other features are a 64 MB SDRAM and an MMC/SD card slot, which are used to store the input and output images. The compression code runs on the C6747 DSP floating point processor core without using any special instructions, such as intrinsic operators (Texas-Instruments 2010).

Processing on the DSP board starts by fetching n out of N number of bands of the hyperspectral image from the MMC/SD card available on the board, which are moved into the local memory (SDRAM). The loaded spectral bands are encoded and stored back to the MMC/SD card along with the output coefficients. This process is repeated for c number of iterations until all N bands are encoded. With limited on-board memory (64 MB), only 16 out of 224 bands of the AVIRIS images and only 49 out of 196 bands of Hyperion hyperspectral images can be loaded into the memory at one time. This corresponds to $c_{min} = 224/16 = 14$ (for AVIRIS) and $c_{min} = 196/49 = 4$ (for Hyperion), which is the smallest number of clusters that can be processed. Therefore, only the numbers of clusters, $c = 14, 16, 28, 32$ and 56 for the AVIRIS images and $c = 4, 7, 14, 28$ and 49 for the Hyperion images can be executed on the DSP due to the memory limitations.

The integer KLT DSP version produced exactly the same output and the same compression ratio results as shown in Table 6 and 7, the only difference being that the DSP implementation started from number of clusters $c = 14$ for AVIRIS and $c = 4$ for Hyperion, rather than from $c = 1$.

Table 11 and 12 show compression latency for the DSP implementation excluding the I/O time. Both datasets have been compressed with similar tile sizes as stated in Section 5.1. Each column in the tables denotes execution time for a different number of clusters, c .

Shaded cells are the latency values corresponding to the highest compression ratio reported in Table 6 and 7. From comparison of Table 11 and 12 with Table 9 and 10, it can be seen that the latency of the integer KLT DSP implementation follows a similar pattern to that shown by the desktop system for larger number of clusters c . Overall, it takes around 3-5 minutes to encode the 224 bands of the AVIRIS images and 0.5-4 minutes for the Hyperion images. This timing is suitable for certain on-board image acquisition scenarios that do not require compression of the satellite imagery continuously in real time.

Table 11. Integer KLT execution time (seconds) on OMAP-L137 for AVIRIS (airborne) datasets with clustering and tiling.

Tile Size	No. of clusters, c (No. of bands/cluster)	14 (16)	16 (14)	28 (8)	32 (7)	56 (4)
64×64	Jasper3	560.210	540.576	227.472	441.728	170.464
	Low2	560.420	540.629	227.463	441.758	170.437
	YellowstoneCal11	559.986	540.743	227.488	441.643	170.488
	YellowstoneCal18	560.553	540.719	227.439	441.692	170.394
128×128	Jasper3	341.470	300.071	222.681	206.477	168.996
	Low2	341.135	300.045	222.603	206.421	168.992
	YellowstoneCal11	341.105	299.96	222.655	206.388	168.875
	YellowstoneCal18	341.075	299.875	222.637	206.335	168.819
256×256	Jasper3	337.427	301.275	222.958	208.432	169.233
	Low2	337.122	301.191	222.893	208.340	169.259
	YellowstoneCal11	337.104	301.163	222.943	208.302	169.303
	YellowstoneCal18	337.086	301.117	222.922	208.244	169.297
512×512	Jasper3	333.240	293.903	220.449	204.624	167.605
	Low2	332.949	293.724	220.283	204.526	167.643
	YellowstoneCal11	332.940	293.788	220.668	204.510	167.818
	YellowstoneCal18	332.931	293.768	220.589	204.409	167.817

Table 12. Integer KLT execution time (seconds) on OMAP-L137 for Hyperion (spaceborne) datasets with clustering and tiling.

Tile Size	No. of clusters, c (No. of bands/cluster)	4 (49)	7 (28)	14 (14)	28 (7)	49 (4)
64×64	Greenland	365.776	139.447	71.862	52.164	37.289
	Boston	365.764	139.587	71.890	52.136	37.387
	Edenton	365.724	139.601	71.904	52.248	37.240
	Portobago	365.736	139.517	71.876	52.276	37.363
128×128	Greenland	248.585	112.292	68.283	51.34	36.837
	Boston	248.611	112.272	68.297	51.325	36.830
	Edenton	248.557	112.263	68.288	51.335	36.826
	Portobago	248.581	112.274	68.278	51.330	36.820
256×256	Greenland	222.695	109.008	67.98	51.247	37.186
	Boston	222.702	109.019	67.99	51.265	37.177
	Edenton	222.704	109.025	67.981	51.262	37.164
	Portobago	222.690	109.016	67.994	51.250	37.188

7. Conclusions

This article reviewed hyperspectral spaceborne missions and their main specifications, including compression capabilities available on board satellites. It is concluded that there are not many missions that support on-board hyperspectral image processing and only three missions, currently operational, have been reported to perform hyperspectral data compression on board. However, details of the compression techniques implemented are not available in the open literature. Future missions will have a greater spectral coverage using more bands at a smaller spectral sampling, which will lead to the generation of even greater amounts of valuable data, increasing further the importance of on-board hyperspectral image compression.

In addition, an investigation into the suitability of the reversible KLT transform, called integer KLT, for lossless inter-band compression in hyperspectral imaging payloads was presented. The results of a comprehensive modelling experiment are given, taking into account the effects of clustering and tiling. It is found that clustering can significantly improve both compression performance and latency of the algorithm. Image tiling, on the other hand, does not markedly affect execution time but it is believed to have an impact on error resilience. However, small tile size combined with a low level of clustering can slow the processing significantly.

The KLT algorithm was prototyped on an embedded platform and performance results were reported. The latency achieved was found to be suitable for certain remote-sensing scenarios. The speed of execution can further be increased through software and hardware optimization. Limitations of the prototyping board were identified, which prevented the testing of all possible combinations in terms of cluster and tile sizes.

In summary, the use of clustering and tiling techniques facilitates the implementation of the computationally intensive integer KLT transform on board remote-sensing satellites. Both clustering and tiling can help to reduce memory usage since they scale down the granularity of the computational process whereby a smaller portion of the hyperspectral cube is processed at each iteration, leading to a smaller buffer size for the overall operation. This 'divide and conquer' approach renders the integer KLT suitable to future hyperspectral missions that will have a much greater number of spectral bands and a larger swathe width than at present.

References

- Abrams, M. 1992. Simulation of ASTER Data Using AVIRIS Images. Paper presented at the Summaries of the Third Annual JPL Airborne Geoscience Workshop, Pasadena, California, June 1-5.
- Aiazzi, B., P. Alba, L. Alparone, and S. Baronti. 1999. "Lossless Compression of Multi/Hyperspectral Imagery Based on a 3-D Fuzzy Prediction." Review of. *IEEE Transactions on Geoscience and Remote Sensing* 37 (5):2287-94.
- Anderson, Christine, Charles S. Vanek, H. Richard Freeman, David Furlong, Alan Kirschbaum, Richard Roy, Peter Wilhelm, and Steve Wander. 1998. *Lewis Spacecraft Mission Failure Investigation Board - Final Report*. Los Angeles, CA: National Aeronautics and Space Administration.
- Aoyanagi, Yoshihide, Shin Satori, Tsuyoshi Totani, Toshihiko Yasunaka, Akihiro Nakamura, and Yusuke Takeuchi. 2010. "Development of Spaceborne Small Hyperspectral sensor HSC-III for Micro Satellite." In *Small Satellite Missions for Earth Observation*, edited by Rainer Sandau, Hans-Peter Roeser and Arnoldo Valenzuela, 331-40. Heidelberg: Springer.
- Aoyanagi, Yoshihide, Tsuyoshi Totani, Kouji Yamaguchi, Norihide Takeyama, and Shin Satori. 2011. Design and Ground Testing of Compact and Versatile Hyperspectral sensor HSC. Paper presented at the 8th IAA (International Academy of Astronautics) Symposium on Small Satellites for Earth Observation, Berlin, Germany, April 4-8.

- Baizert, P., M. R. Pickering, and M. J. Ryan. 2001. Compression of Hyperspectral Data by Spatial/Spectral Discrete Cosine Transform. Paper presented at the IEEE International Conference on Geoscience and Remote Sensing Symposium, 2001 (IGARSS 2001), Sydney, Australia, July 9-13.
- Barducci, A., P. Marcoionni, and I. Pippi. 2006. "Recent Advance in Earth Remote Sensing: Fourier Transform Stationary Hyperspectral Imagers." Review of *Annals of Geophysics* 49.
- Barnhart, David J., Tanya Vladimirova, Adam M. Baker, and Martin N. Sweeting. 2009. "A Low-Cost Femtosatellite to Enable Distributed Space Missions." Review of *Acta Astronautica* 64 (11-12):1123-43.
- Bisser, K. "Compact Reconnaissance Imaging Spectrometer for Mars Website." Accessed 10 Dec 2011. <http://crism.jhuapl.edu/>.
- Bergeron, M., A. Hollinger, and P. Oswald. "The Hyperspectral Environment and Resource Observer (HERO) Mission." Accessed 14 July 2011. http://carms.geog.uvic.ca/HSIWSPresentations/Monday_am/4_Bergeron_HERO.ppt.
- Bergeron, M., A. Hollinger, K. Staenz, M. Maszkiewicz, R.A. Neville, S.E. Qian, and D.G. Goodenough. 2008. "Hyperspectral Environment and Resource Observer (HERO) Mission." Review of *Canadian Journal of Remote Sensing* 34 (1):S1-S11.
- Bermyn, Jo. 2000. "PROBA - PProject for On-Board Autonomy." Review of *Journal of Air & Space Europe* 2 (1):70-6.
- Bezy, J. L., G. Gourmelon, R. Bessudo, G. Baudin, H. Sontag, and S. Weiss. 1999. The ENVISAT Medium Resolution Imaging Spectrometer (MERIS). Paper presented at the IEEE International Conference on Geoscience and Remote Sensing Symposium, 1999 (IGARSS 1999), Hamburg, Germany, Jun 28-Jul 2.
- Bibring, J. P., A. Soufflot, M. Berthé, Y. Langevin, B. Gondet, P. Drossart, M. Bouyé, M. Combes, P. Puget, A. Semery, G. Bellucci, V. Formisano, V. Moroz, V. Kottsov, OMEGA Co-I Team: G. Bonello, S. Erard, O. Forni, A. Gendrin, N. Manaud, F. Poulet, G. Poulleau, T. Encrenaz, T. Fouchet, R. Melchiori, F. Altieri, N. Ignatiev, D. Titov, L. Zasova, A. Coradini, F. Capacionni, P. Cerroni, S. Fonti, N. Mangold, P. Pinet, B. Schmitt, C. Sotin, E. Hauber, H. Hoffmann, R. Jaumann, U. Keller, R. Arvidson, J. Mustard, and F. Forget. 2004. *OMEGA: Observatoire pour la Minéralogie, l'Eau, les Glaces et l'Activité*. Vol. 1240, *Mars Express: The Scientific Payload*. Noordwijk, Netherlands: ESA Publ. Division.
- Blanes, Ian, and Joan Serra-Sagrístà. 2009. Clustered Reversible-KLT for Progressive Lossy-to-Lossless 3D Image Coding. Paper presented at the Data Compression Conference, 2009 (DCC '09), Snowbird, Utah, March 16-18.
- Bochkanov, S. A. "ALGLIB - Open Source." Accessed 10 Dec 2011. <http://www.alglib.net/>.
- Bonello, Guillaume, Jean-Pierre Bibring, François Poulet, Aline Gendrin, Brigitte Gondet, Yves Langevin, and Sergio Fonti. 2004. "Visible and Infrared Spectroscopy of Minerals and Mixtures with the OMEGA/MARS-EXPRESS Instrument." Review of *Planetary and Space Science* 52 (1-3):133-40.
- Borengasser, Marcus, William S. Hungate, and Russell Watkins. 2008a. *Hyperspectral Remote Sensing: Principles and Applications*. Edited by Qihao Weng. Boca Raton, FL: Taylor & Francis Group.
- . 2008b. "Imaging Spectrometers: Operational Considerations." In *Hyperspectral Remote Sensing: Principles and Applications*, edited by Qihao Weng, 17. Boca Raton, FL: Taylor & Francis Group.
- Boucher, Marc. 2001. "Taurus Launch ends in Failure, QuikTOMS and OrbView-4 Lost." In *SpaceRef*.
- Bowles, J.H., J.A. Antoniadis, M.M. Baumbach, D. Hass, and P.J. Palmadesso. 1996. Effects of Spectral Resolution and Number of Wavelength Bands in Analysis of a Hyperspectral Data Set Using NRL's ORASIS Algorithm. Paper presented at the Proceedings of SPIE in Hyperspectral Remote Sensing and Applications Vol. 2821, Denver, CO, November 6.
- Buckingham, R., and K. Staenz. 2008. "Review of Current and Planned Civilian Space Hyperspectral Sensors for EO." Review of *Canadian Journal of Remote Sensing* 34 (1):S187-S97.
- Buckingham, R., K. Staenz, and A. Hollinger. 2002. "A Review of Canadian Airborne and Space Activities in Hyperspectral Remote Sensing." Review of *Canadian Aeronautics and Space Journal* 48 (1):115-21.

- Buckner, J.L. "HyspIRI Technology Investment Overview." Accessed 10 Dec 2011. http://decadal.gsfc.nasa.gov/documents/HyspIRI_Technology_Investments.pdf.
- CCSDS. 2012a. *Lossless Data Compression - Recommended Standard (CCSDS 121.0-B-2)*. Washington DC, USA: CCSDS Secretariat, NASA.
- . 2012b. *Lossless Multispectral & Hyperspectral Image Compression - Recommended Standard (CCSDS 123.0-B-1)*. Washington DC, USA: CCSDS Secretariat, NASA.
- Christophe, E., C. Mailhes, and P. Duhamel. 2008. "Hyperspectral Image Compression: Adapting SPIHT and EZW to Anisotropic 3-D Wavelet Coding." Review of. *IEEE Transactions on Image Processing* 17 (12):2334-46.
- Cutter, M., and M. Sweeting. 2007. A Hyperspectral Imaging Mission for Small Satellites - Five Years Orbit Experience. Paper presented at the 3rd International Conference on Recent Advances in Space Technologies, 2007 (RAST '07), Istanbul, Turkey, June 14-16.
- Davis, T.M., and S.D. Straight. 2006. Development of the Tactical Satellite 3 for Responsive Space Missions. Paper presented at the 4th Responsive Space Conference, Los Angeles, USA, April 24-27.
- Dubock, P.A., F. Spoto, J. Simpson, D. Spencer, E. Schutte, and H. Sontag. June 2001. *The Envisat Satellite and Its Integration, ESA Bulletin No 1006*. Noordwijk, Netherlands: European Space Agency.
- eoPortal. "eoPortal: Sharing Earth Observation Resources." Accessed 10 Dec 2011. <http://directory.eoportal.org>.
- ESA. "ESA - Mars Express." Accessed 10 Dec 2011. http://www.esa.int/SPECIALS/Mars_Express/.
- . "ESA declares end of mission for Envisat." Accessed 3rd June 2012. http://www.esa.int/esaCP/SEM1XSXSWT1H_index_0.html.
- Fisher, J., J.A. Antoniadis, C. Rollins, and L.Q. Xiang. 1998. Hyperspectral Imaging Sensor for the Coastal Environment. Paper presented at the Proceedings of SPIE in International Optical Design Conference 1998 Vol. 3482, Kona, HI, September 21.
- Frazier, S. "MODIS Website." Accessed 1 June 2012. <http://modis.gsfc.nasa.gov/about/electrsys.php>.
- Freeman, J., C. Rudder, and P. Thomas. 2000. MightySat II: On-orbit Lab Bench for Air Force Research Laboratory. Paper presented at the Proceedings of the 14th Annual AIAA/USU Conference on Small Satellites, Logan, Utah, USA, August 21-24.
- Galeazzi, C., A. Sacchetti, A. Cisbani, and G. Babini. 2008. The PRISMA Program. Paper presented at the IEEE International Conference on Geoscience and Remote Sensing Symposium, 2008 (IGARSS 2008), Boston, USA, July 7-11.
- Galli, L., and S. Salzo. 2004. Lossless Hyperspectral Compression Using KLT. Paper presented at the IEEE International Conference on Geoscience and Remote Sensing Symposium, 2004 (IGARSS 2004), Anchorage, Alaska, USA, September 20-24.
- Gersho, A., and R.M. Gray. 1992. *Vector Quantization and Signal Compression*. Norwell, MA: Kluwer Academic Publishers.
- Green, R. O., G. Asner, S. Ungar, and R. Knox. 2008. NASA Mission to Measure Global Plant Physiology and Functional Types. Paper presented at the IEEE Aerospace Conference, 2008, Big Sky, MT, USA, March 1-8.
- Green, Robert O., Michael L. Eastwood, Charles M. Sarture, Thomas G. Chrien, Mikael Aronsson, Bruce J. Chippendale, Jessica A. Faust, Betina E. Pavri, Christopher J. Chovit, Manuel Solis, Martin R. Olah, and Orlesa Williams. 1998. "Imaging Spectroscopy and the Airborne Visible/Infrared Imaging Spectrometer (AVIRIS)." Review of. *Remote Sensing of Environment* 65 (3):227-48.
- Guelman, M., and F. Ortenberg. 2009. "Small Satellite's Role in Future Hyperspectral Earth Observation Missions." Review of. *Acta Astronautica* 64 (11-12):1252-63.
- Hao, P., and Q. Shi. 2001. "Matrix Factorizations for Reversible Integer Mapping." Review of. *IEEE Transactions on Signal Processing* 49 (10):2314-24.
- . 2003. Reversible Integer KLT for Progressive-to-Lossless Compression of Multiple Component Images. Paper presented at the Proceedings of the International Conference on Image Processing, 2003 (ICIP 2003), Barcelona, Spain, September 14-17.
- Heffernan, K. J., J. E. Heiss, J. D. Boldt, E. Hugo Darlington, K. Peacock, T. J. Harris, and M. J. Mayr. 1996. "The UVISI Instrument." Review of. *Johns Hopkins APL Technical Digest* 17 (2):198-214.

- Hofer, S., K.-P. Förster, B. Sang, T. Stuffer, B. Penné, M. Kassebom, H. Kaufmann, A. Müller, and C. Chlebek. 2010. EnMAP Hyperspectral Mission - The Space Segment. Paper presented at the Proceedings of the Hyperspectral Workshop 2010, Frascati, Italy, March 17-19.
- Hook, Simon J. "HyTES: A Hyperspectral Thermal Emission Spectrometer for HypsIRI-TIR Science." Accessed 10 Dec 2011. <http://airbornescience.jpl.nasa.gov/hytes/>.
- Hook, Simon J., Bjorn T. Eng, Sarath D. Gunapala, Cory J. Hill, William R. Johnson, Andrew U. Lamborn, Pantazis Mouroulis, Jason M. Mumolo, Christopher G. Paine, Vincent J. Realmuto, and Daniel W. Wilson. 2010. QWEST and HyTES: Two New Hyperspectral Thermal Infrared Imaging Spectrometers for Earth Science. Paper presented at the ESTF (Earth Science Technology Forum) 2010, Arlington, VA, USA, June 22-24.
- Hopson, B., K. Benkrid, D. Keymeulen, and N. Aranki. 2012. Real-time CCSDS Lossless Adaptive Hyperspectral Image Compression on Parallel GPGPU & Multicore Processor Systems. Paper presented at the NASA/ESA Conference on Adaptive Hardware and Systems (AHS), 2012, Erlangen, Germany, June 25-28.
- Huebschman, R. K. . 1996. "The MSX Spacecraft System Design." Review of. *Johns Hopkins APL Technical Digest* 17 (1):41-8.
- Hunt, S., and L. S. Rodriguez. 2004. Fast Piecewise Linear Predictors for Lossless Compression of Hyperspectral Imagery. Paper presented at the IEEE International Conference on Geoscience and Remote Sensing Symposium, 2004 (IGARSS 2004), Anchorage, Alaska, USA, September 20-24.
- ITT. "ENVI Tutorial: Hyperspectral Signature and Spectral Resolution." Accessed 10 Dec 2011. www.exelisvis.com/portals/0/tutorials/envi/Signatures_Spectral_Res.pdf.
- Jing, Zhang, J. E. Fowler, and Liu Guizhong. 2008. "Lossy-to-Lossless Compression of Hyperspectral Imagery Using Three-Dimensional TCE and an Integer KLT." Review of. *IEEE Geoscience and Remote Sensing Letters* 5 (4):814-8.
- Johnson, William R., Simon J. Hook, Pantazis Mouroulis, Daniel W. Wilson, Sarath D. Gunapala, Cory J. Hill, Jason M. Mumolo, and Bjorn T. Eng. 2009. "Quantum Well Earth Science Testbed." Review of. *Infrared Physics & Technology* 52 (6):430-3. doi: 10.1016/j.infrared.2009.05.006.
- Kalman, L.S., and G.R. Pelzer. 1993. "Simulation of Landsat Thematic Mapper Imagery Using AVIRIS Hyperspectral Imagery." In *Summaries of the Fourth Annual JPL Airborne Geoscience Workshop*, 97-100. Pasadena, California: Jet Propulsion Laboratory, JPL Publ. 93-26.
- Khayam, S.A. 2003. *The Discrete Cosine Transform (DCT): Theory and Application*. East Lansing, MI: Michigan State University.
- Kiely, A. B., and M. A. Klimesh. 2009. "Exploiting Calibration-Induced Artifacts in Lossless Compression of Hyperspectral Imagery." Review of. *IEEE Transactions on Geoscience and Remote Sensing* 47 (8):2672-8.
- Lee, H. S., N. H. Younan, and R. L. King. 2002. Hyperspectral Image Cube Compression Combining JPEG-2000 and Spectral Decorrelation. Paper presented at the IEEE International Conference on Geoscience and Remote Sensing Symposium, 2002 (IGARSS 2002), Toronto, Canada, June 24-28.
- Lei, Wang, Wu Jiaji, Jiao Licheng, and Shi Guangming. 2009. 3D Medical Image Compression Based on Multiplierless Low-Complexity RKLT and Shape-Adaptive Wavelet Transform. Paper presented at the 16th IEEE International Conference on Image Processing 2009 (ICIP 2009), Cairo, Egypt, November 7-12.
- Lillesand, Thomas M., Ralph W. Kiefer, and Jonathan W. Chipman. 2008. *Remote Sensing and Image Interpretation*. 6 ed. Hoboken, NJ: John Wiley & Sons, Inc.
- Liu, G., and F. Zhao. 2008. "Efficient Compression Algorithm for Hyperspectral Images Based on Correlation Coefficients Adaptive 3D Zerotree Coding." Review of. *IET Image Processing* 2 (2):72-82.
- Louet, J. "The Envisat Mission and System." Accessed 10 Dec 2011. http://www.esa.int/esapub/bulletin/bullet106/bul106_1.pdf.
- Marshall, D. 1995. Small Spacecraft Technology Initiative - Lewis Spacecraft. Paper presented at the AIAA Space Programs and Technologies Conference, Huntsville, Alabama, USA, September 26-28.
- Mat Noor, N. R., and T. Vladimirova. 2011. "Integer KLT Design Space Exploration for Hyperspectral Satellite Image Compression." In *Lecture Notes in Computer Science* -

- Convergence and Hybrid Information Technology*, edited by Geuk Lee, Daniel Howard and Dominik Slezak, 661-8. Springer Berlin / Heidelberg.
- Mat Noor, N. R., T. Vladimirova, and M. Sweeting. 2010. High Performance Lossless Compression for Hyperspectral Satellite Imagery. Paper presented at the UK Electronics Forum, Newcastle University, UK, June 30- July 1.
- Mather, P.M. 2004. *Computer Processing of Remotely-Sensed Images*. West Sussex, England: John Wiley & Sons Inc.
- Melchiorri, R., P. Drossart, T. Fouchet, B. Bézard, F. Forget, A. Gendrin, J. P. Bibring, and N. Manaud. 2006. "A Simulation of the OMEGA/Mars Express Observations: Analysis of the Atmospheric Contribution." Review of. *Planetary and Space Science* 54 (8):774-83.
- Merton, J., and J. Huntington. 1999. Early Simulation Results of the ARIES-1 Satellite Sensor for Multi-Temporal Vegetation Research Derived from AVIRIS. Paper presented at the Proceedings of the Eighth Annual JPL Airborne Earth Science Workshop, NASA, JPL., Pasadena, CA, February 8-14.
- Michel, S., M.J. Lefevre-Fonollosa, and S. Hosford. 2010. HYPXIM-A Hyperspectral Satellite Defined for Science, Security and Defence Users. Paper presented at the Proceedings of the Hyperspectral Workshop 2010, Frascati, Italy, March 17-19.
- Mielikainen, J., and P. Toivanen. 2003. "Clustered DPCM for the Lossless Compression of Hyperspectral Images." Review of. *IEEE Transactions on Geoscience and Remote Sensing* 41 (12):2943-6.
- Murchie, S., R. Arvidson, P. Bedini, K. Beisser, J. P. Bibring, J. Bishop, J. Boldt, P. Cavender, T. Choo, R. T. Clancy, E. H. Darlington, D. Des Marais, R. Espiritu, D. Fort, R. Green, E. Guinness, J. Hayes, C. Hash, K. Heffernan, J. Hemmler, G. Heyler, D. Humm, J. Hutcherson, N. Izenberg, R. Lee, J. Lees, D. Lohr, E. Malaret, T. Martin, J. A. McGovern, P. McGuire, R. Morris, J. Mustard, S. Pelkey, E. Rhodes, M. Robinson, T. Roush, E. Schaefer, G. Seagrave, F. Seelos, P. Silverglate, S. Slavney, M. Smith, W. J. Shyong, K. Strohhahn, H. Taylor, P. Thompson, B. Tossman, M. Wirzburger, and M. Wolff. 2007. "Compact Reconnaissance Imaging Spectrometer for Mars (CRISM) on Mars Reconnaissance Orbiter (MRO)." Review of. *J. Geophys. Res.* 112 (E5):E05S3. doi: 10.1029/2006je002682.
- NASA-JPL. "Hyperspectral Image Compression - AVIRIS & Hyperion Raw Data." Accessed 10 Dec 2011. <http://compression.jpl.nasa.gov/hyperspectral/>.
- . "Ordering Free AVIRIS Standard Data Products." Accessed 10 Dec 2011. <http://aviris.jpl.nasa.gov/html/aviris.freedata.html>.
- Navulur, Kumar. 2007. *Multispectral Image Analysis Using the Object-Oriented Paradigm*. Boca Raton, FL: Taylor & Francis Group.
- Nefian, A. V., and M. H. Hayes, III. 1998. Face Detection and Recognition Using Hidden Markov Models. Paper presented at the International Conference on Image Processing, 1998 (ICIP 98), Chicago, Illinois, USA, October 4-7.
- Palmadesso, P.J., J. Antoniadis, M. Baumbach, J. Bowles, and L. Rickard. 1995. Use of Filter Vectors and Fast Convex Set Methods in Hyperspectral Analysis. Paper presented at the Proceedings of the International Symposium on Spectral Sensing Research, Melbourne, Australia, November 26-December 1.
- Paolo, M., D. Michele, G. Lorenzo, P. Beatrice, and F. Enrico. 2010. PRISMA Payload. Paper presented at the Proceedings of the Hyperspectral Workshop 2010, Frascati, Italy, March 17-19.
- Parkinson, C. L. 2003. "Aqua: An Earth-Observing Satellite Mission to Examine Water and Other Climate Variables." Review of. *IEEE Transactions on Geoscience and Remote Sensing* 41 (2):173-83.
- Pearlman, J. S., P. S. Barry, C. C. Segal, J. Shepanski, D. Beiso, and S. L. Carman. 2003. "Hyperion, A Space-Based Imaging Spectrometer." Review of. *IEEE Transactions on Geoscience and Remote Sensing* 41 (6):1160-73.
- Pearlman, J., C. Segal, L.B. Liao, S. L. Carman, M.A. Folkman, W. Browne, L. Ong, and S. G. Ungar. 2000. Development and Operations of the EO-1 Hyperion Imaging Spectrometer. Paper presented at the Proceedings of SPIE in Earth Observing Systems Vol. 4135, San Diego, USA, November 15.
- Penna, B., T. Tillo, E. Magli, and G. Olmo. 2005. Embedded Lossy to Lossless Compression of Hyperspectral Images Using JPEG 2000. Paper presented at the IEEE International Conference

- on Geoscience and Remote Sensing Symposium, 2005 (IGARSS 2005), Seoul, Korea, July 25-29.
- . 2006. A New Low Complexity KLT for Lossy Hyperspectral Data Compression. Paper presented at the IEEE International Conference on Geoscience and Remote Sensing Symposium, 2006 (IGARSS 2006), Denver, Colorado, USA, July 31-August 4.
- Peter, W.T. Yuen, and B. Gary. 2006. Hyperspectral Algorithm Development for Military Applications: A Multiple Fusion Approach. Paper presented at the 3rd Electro-Magnetic Remote Sensing Defence Technology Centres (EMRS DTCs) Technical Conference, Edinburgh, UK, July 13-14.
- Pickering, M. R., and M. J. Ryan. 2000. Compression of Hyperspectral Data Using Vector Quantisation and The Discrete Cosine Transform. Paper presented at the IEEE International Conference on Image Processing, 2000 (ICIP 2000), Vancouver, Canada, September 10-13.
- Pickering, Mark R., and Michael J. Ryan. 2006. "Chapter 1: An Architecture for the Compression of Hyperspectral Imagery." In *Hyperspectral Data Compression*, edited by G. Motta, F. Rizzo and J. A. Storer, 1-34. New York, USA.: Springer Science+Business Media, Inc.
- Przyborski, P. "NASA: TERRA." Accessed 24 August 2011. <http://terra.nasa.gov/>.
- Qian, Du, and J. E. Fowler. 2007. "Hyperspectral Image Compression Using JPEG2000 and Principal Component Analysis." Review of. *IEEE Geoscience and Remote Sensing Letters* 4 (2):201-5.
- Quintiliano, P., and A. Santa-Rosa. 2003. Detection of Streets Based On KLT Using IKONOS Multispectral Images. Paper presented at the 2nd GRSS/ISPRS Joint Workshop on Remote Sensing and Data Fusion over Urban Areas, 2003 (URBAN 2003), Berlin, Germany, May 22-23.
- Rabbani, Majid, and Paul W. Jones. 1991. *Digital Image Compression Techniques*. Vol. TT7. Bellingham, WA: SPIE - The International Society for Optical Engineering.
- Rabideau, G., D. Tran, S. Chien, B. Cichy, R. Sherwood, D. Mandl, S. Frye, S. Shulman, J. Swaczkowski, D. Boyer, and J. Van Gaasbeck. 2006. Mission Operations of Earth Observing-1 with Onboard Autonomy. Paper presented at the Second IEEE International Conference on Space Mission Challenges for Information Technology, 2006 (SMC-IT 2006), Pasadena, California, USA, July 17-20.
- Read, Trevor. "PROBA Payload Processing." Accessed 4 May 2010. http://www.chris-proba.org.uk/WS2003/PROBA_Payload_Processing_TRead.ppt.
- Rice, R., and J. Plaunt. 1971. "Adaptive Variable-Length Coding for Efficient Compression of Spacecraft Television Data." Review of. *IEEE Transactions on Communication Technology* 19 (6):889-97.
- Richards, J. 1993. *Remote Sensing Digital Image Analysis: An Introduction*. 2nd. ed. New York: Springer-Verlag.
- Roger, R. E., and M. C. Cavenor. 1996. "Lossless Compression of AVIRIS Images." Review of. *IEEE Transactions on Image Processing* 5 (5):713-9.
- Ryan, M. J., and J. F. Arnold. 1997a. "The Lossless Compression of AVIRIS Images by Vector Quantization." Review of. *IEEE Transactions on Geoscience and Remote Sensing* 35 (3):546-50.
- Ryan, Michael J., and John F. Arnold. 1997b. "Lossy Compression of Hyperspectral Data Using Vector Quantization." Review of. *Remote Sensing of Environment* 61 (3):419-36.
- Sacchetti, A., C. Galeazzi, A. Cisbani, and G. Babini. 2009. The Italian Precursor of An Operational Hyperspectral Imaging Mission. Paper presented at the Proceedings of the 7th IAA Symposium on Small Satellites for Earth Observation, Berlin, Germany, May 4-7.
- Saghri, J. A., A. G. Tescher, and J. T. Reagan. 1995. "Practical Transform Coding of Multispectral Imagery." Review of. *IEEE Signal Processing Magazine* 12 (1):32-43.
- Salomon, D. 2007. *Data Compression: The Complete Reference*. 4th ed. London: Springer Science+Business Media, LLC.
- Santa-Cruz, Diego, Touradj Ebrahimi, Joel Askelof, Mathias Larsson, and Charilaos A. Christopoulos. 2000. JPEG2000 Still Image Coding Versus Other Standards. Paper presented at the Proceedings of SPIE in Applications of Digital Image Processing XXIII Vol. 4115, San Diego, CA, December 28.
- Schaepman, Michael E. 2007. "Spectrodirectional Remote Sensing: From Pixels to Processes." Review of. *International Journal of Applied Earth Observation and Geoinformation* 9 (2):204-23.

- Schaepman, Michael E., Susan L. Ustin, Antonio J. Plaza, Thomas H. Painter, Jochem Verrelst, and Shunlin Liang. 2009. "Earth System Science Related Imaging Spectroscopy - An Assessment." Review of *Remote Sensing of Environment* 113:123-37.
- Schoeberl, M. R., A. R. Douglass, E. Hilsenrath, P. K. Bhartia, R. Beer, J. W. Waters, M. R. Gunson, L. Froidevaux, J. C. Gille, J. J. Barnett, P. F. Levelt, and P. DeCola. 2006. "Overview of the EOS Aura Mission." Review of *IEEE Transactions on Geoscience and Remote Sensing* 44 (5):1066-74.
- Shippert, P. 2003. "Introduction to Hyperspectral Image Analysis." Review of *Online Journal of Space Communication - Remote Sensing of Earth via Satellite* (Issue No. 3).
- Skullney, W. E., Jr. H. M. Kreitz, M. J. Harold, S. R. Vernon, T. M. Betenbaugh, T. J. Hartka, D. F. Persons, and E. D. Schaefer. 1996. "Structural Design of the MSX Spacecraft." Review of *Johns Hopkins APL Technical Digest* 17 (1):59-76.
- Smith, T., and J. Kessler. 1999. "Earth Orbiter 1 - Wideband Advanced Recorder and Processor (WARP)."
- Stott, D. D., R. K. Burek, P. Eisenreich, J. E. Kroutil, P. D. Schwartz, and G. F. Sweitzer. 1996. "The MSX Command and Data Handling System." Review of *Johns Hopkins APL Technical Digest* 17 (1):143-51.
- Stoffler, T., C. Kaufmann, S. Hofer, K. P. Förster, G. Schreier, A. Mueller, A. Eckardt, H. Bach, B. Penné, U. Benz, and R. Haydn. 2007. "The EnMAP Hyperspectral Imager - An Advanced Optical Payload for Future Applications in Earth Observation Programmes." Review of *Acta Astronautica* 61 (1-6):115-20.
- Taubman, D. "Kakadu Software." Accessed 10 Dec 2011. <http://www.kakadusoftware.com/>.
- Texas-Instruments. "TMS320C6000 Programmer's Guide (SPRU198K)." Texas Instrument, Accessed 10 Dec 2011. <http://www.ti.com/lit/ug/spru198k/spru198k.pdf>.
- Thyagarajan, K., and D. V. A. Raghava Murthy. 2009. "Micro- and Mini-Satellites of ISRO - Technology and Applications." Review of *Acta Astronautica* 65 (9-10):1375-82.
- Troxel, I. A., M. Fehringer, and M. T. Chenoweth. 2008a. Achieving Multipurpose Space Imaging with the ARTEMIS Reconfigurable Payload Processor. Paper presented at the IEEE Aerospace Conference, 2008 Big Sky, MT, March 1-8.
- Troxel, I.A., M. Fehringer, and M.T. Chenoweth. 2008b. Achieving Multipurpose Space Imaging with the ARTEMIS Reconfigurable Payload Processor. Paper presented at the Military and Aerospace Programmable Logic Devices (MAPLD) Conference, Annapolis, MD, USA, September 16-18.
- Tyler, S. R., and P. Varanasi. 2001. The Relationship Between Ground Data Systems and Flight Operations for the Aura Project TES Instrument. Paper presented at the IEEE Proceedings of Aerospace Conference, 2001, Big Sky, Montana, USA, March 10-17.
- Ungar, S. G., J. S. Pearlman, J. A. Mendenhall, and D. Reuter. 2003. "Overview of the Earth Observing One (EO-1) Mission." Review of *IEEE Transactions on Geoscience and Remote Sensing* 41 (6):1149-59.
- US Geological Survey. "USGS EO-1 Website." Accessed 3 Oct 2012. <http://eo1.usgs.gov/>.
- USGS. "Hyperion Archive Scenes." Accessed 18 May 2012. <http://eo1.usgs.gov/acquisition/hyperion>.
- Vincent, W. S. 1999. Data Handling for the Navy's Hyperspectral Imaging Satellite-NEMO. Paper presented at the IEEE Aerospace Conference Proceedings, Snowmass at Aspen, CO, USA, March 7.
- Viotti, M. "Mars Exploration." Accessed 10 Dec 2011. <http://marsprogram.jpl.nasa.gov>.
- Vladimirova, T., M. Meerman, and A. Curiel. 2006. On-Board Compression of Multispectral Images for Small Satellites. Paper presented at the IEEE International Conference on Geoscience and Remote Sensing Symposium, 2006 (IGARSS 2006), Denver, Colorado, USA, July 31-August 4.
- Vladimirova, T., and A. Steffens. 2005. Compression of Multispectral Images On-Board Observation Satellites. Paper presented at the Proceedings of the International Conference "Space, Ecology, Safety" (SES '05), Varna, Bulgaria, June 10-13.
- Wander, S. 2007. "Lewis Spins Out of Control." Review of *NASA System Failure Case Studies* 1 (8):4.
- Wang, Honqiang, and Khalid Sayood. 2006. "Chapter 2: Lossless Predictive Compression of Hyperspectral Images." In *Hyperspectral Data Compression*, edited by G. Motta, F. Rizzo and J. A. Storer, 35-55. New York: Springer US.

- Wetzel, M. A. 1995. "Technical Note Simulation of Radiances for Future AVHRR Platforms with the AVIRIS Spectral Radiometer." Review of. *International Journal of Remote Sensing* 16 (6):1167 - 77.
- Willart Soufflet, V., and R. Santer. 1993. Using AVIRIS for In-Flight Calibration of the Spectral Shifts of SPOT HRV and of AVHRR. Paper presented at the Summaries of the Fourth Annual JPL Airborne Geoscience Workshop, Pasadena, California, October 25.
- Willoughby, C. T., J. Marmo, and M. A. Folkman. 1996. Hyperspectral Imaging Payload for the NASA Small Satellite Technology Initiative Program. Paper presented at the Proceedings of the IEEE Aerospace Applications Conference, 1996, Aspen, CO, USA, February 3-10.
- Wilson, J. "NASA - Ozone Monitoring Instrument (OMI)." Accessed 10 Dec 2011. http://www.nasa.gov/mission_pages/aura/spacecraft/omi.html.
- Wilson, Tom, and Rebecca Baugh. 1999. "Naval EarthMap Observer (NEMO) Program and the Naval Space Science and Technology Program Office." Review of. *Acta Astronautica* 44 (7-12):675-83.
- Writers, Staff. 2012. "ATK Announces Retirement of TacSat-3 Satellite." In *Space Daily*. Arlington, VA: Space Media Network.
- Xin, Luo, Guo Lei, and Liu Zhen. 2007a. Lossless Compression of Hyperspectral Imagery Using Integer Principal Component Transform and 3-D Tarp Coder. Paper presented at the Eighth ACIS International Conference on Software Engineering, Artificial Intelligence, Networking, and Parallel/Distributed Computing, 2007 (SNPD 2007), Qingdao, China, July 30-August 1.
- . 2007b. Reversible Integer Principal Component Transform for Hyperspectral Imagery Lossless Compression. Paper presented at the IEEE International Conference on Control and Automation, 2007 (ICCA 2007), Guangzhou, China, May 30-June 1.
- Xiong, X., N. Che, and W. L. Barnes. 2006. "Terra MODIS On-Orbit Spectral Characterization and Performance." Review of. *IEEE Transactions on Geoscience and Remote Sensing* 44 (8):2198-206.
- Yarbrough, S.T., T.R. Caudill, E.T. Kouba, V. Osweiler, J. Arnold, R. Quarles, J. Russell, L.J. Otten, B.A. Jones, A. Edwards, J. Lane, A.D. Meigs, R.B. Lockwood, and P.S. Armstrong. 2002. MightySat II.1 Hyperspectral Imager: Summary of On-Orbit Performance. Paper presented at the Proceedings of SPIE in Imaging Spectrometry VII Vol. 4480, San Diego, CA, January 21.
- Ying, Liu, and W. A. Pearlman. 2007. Multistage Lattice Vector Quantization for Hyperspectral Image Compression. Paper presented at the Conference Record of the Forty-First Asilomar Conference on Signals, Systems and Computers, 2007 (ACSSC 2007), Pacific Grove, USA, November 4-7.
- Yodchanan, W. 2008. Lossless Compression for 3-D MRI Data Using Reversible KLT. Paper presented at the International Conference on Audio, Language and Image Processing, 2008 (ICALIP 2008) Shanghai, China, July 7-9.
- Yodchanan, W., S. Oraintara, T. Tanaka, and K. R. Rao. 2006a. Lossless Multi-Channel EEG Compression. Paper presented at the IEEE International Symposium on Circuits and Systems, 2006 (ISCAS 2006), Island of Kos, Greece, May 21-24.
- Yodchanan, W., O. Soontorn, and K. R. Rao. 2006b. Integer Sub-Optimal Karhunen-Loeve Transform for Multi-channel Lossless EEG Compression. Paper presented at the 14th European Signal Processing Conference, Florence, Italy, September 4-8.
- Yu, Guoxia, Tanya Vladimirova, and Martin N. Sweeting. 2009. "Image Compression Systems On Board Satellites." Review of. *Acta Astronautica* 64 (9-10):988-1005.
- Zhang, Hao, Heng-jia Song, and Bo-chun Yu. 2011. Application of Hyper Spectral Remote Sensing for Urban Forestry Monitoring in Natural Disaster Zones. Paper presented at the International Conference on Computer and Management 2011 (CAMAN 2011), Wuhan, China, May 19-21.
- Zhang, Jing, James E. Fowler, Nicolas H. Younan, and Guizhong Liu. 2009. Evaluation of JP3D for Lossy and Lossless Compression of Hyperspectral Imagery. Paper presented at the IEEE International Geoscience and Remote Sensing Symposium, 2009 (IGARSS 2009), Capetown, South Africa, July 12-17.
- Zhou, Z., J. Liu, and J. Tian. 2006. Real-time Hyperspectral Image Cube Compression Combining Adaptive Classification and Partial Transform Coding. Paper presented at the 8th International Conference on Signal Processing, 2006 (ICSP 2006), Beijing, China, November 16-20.